Automatic features identification with Infrared Thermography in Fever Screening

by

Vijaykumar Surabhi

The thesis submitted to the

Faculty of Graduate and Postdoctoral Studies

In Partial Fulfilment of the Requirements

For the Degree of

Master of Applied Science in Biomedical Engineering

Department of Mechanical Engineering

University of Ottawa

Abstract

The goal of this thesis is to develop an algorithm to process infrared images and achieve automatic identification of moving subjects with fever. The identification is based on two main features: the distinction between the geometry of a human face and other objects in the field of view of the camera, and the temperature of the radiating object. Infrared thermography is a remote sensing technique used to measure temperatures based on emitted infrared radiation. Applications include fever screening in major public places such as airports and hospitals. Current accepted practice of screening requires people to stay in a line and temperature measurements are carried out for one person at a time. However in the case of mass screening of moving people the accuracy of the measurements is still under investigation.

An algorithm constituting of image processing to threshold objects based on the temperature, template matching and hypothesis testing is proposed to achieve automatic identification of fever subjects. The algorithm was first tested on training data to obtain a threshold value (used to discriminate between face and non face shapes) corresponding to a false detection rate of 5%, which in turn corresponds to 85% probability of detection using Neyman-Pearson criterion.

By testing the algorithm on several simulated and experimental images (which reflect relevant scenarios characterizing crowded places) it is observed that it can be beneficially implemented to introduce automation in the process of detecting moving subjects with fever.

Acknowledgments

I would like to express my gratitude to my supervisor Dr. Dan Necsulescu and to my co-supervisor Dr. Davide Spinello for the guidance, support, patience and generous help throughout my graduate study and more importantly, for the vision of finding such an interesting and rewarding thesis topic. Special thanks to my parents and all my friends for being there for me and their continuous encouragement is the motivation for the accomplishment of the thesis.

Table of contents

Table of contents

List of figures

List of figures

List of figures

List of tables

CHAPTER 1

1 Introduction

1.1 Overview

Infrared thermography is an imaging technique used for constructing thermal maps of emitting objects by detecting the infrared radiation emitted from the surface and by converting it into measurable signal [1]. It has been used in a wide range of applications in the field of medicine, which includes measurement of human body temperature [2], skin hemodynamics, hands temperature measurement, brain and neurosurgery and breast cancer [2]. After the outbreak of severe acute respiratory syndrome (SARS) in 2003, it has been widely used for temperature monitoring in major crowded places like health care institutions, airports, and other private establishments to stop the spread of disease [3].

According to ISO/IEC joint working committee, practice of fever screening using infrared thermography in major public places is accepted and validated only if the person to be scrutinized stands still in front of the camera and the camera aims directly at the person’s face [4]. This procedure is difficult, time consuming and ultimately not practicable for mass screening of people in airports and hospitals. The opinion of the committee is that the use of thermal imaging for screening of transiting people would not produce reliable results and gave recommendations for further research. Data and publications are needed to substantiate the validity of the screening technique and reliability of the screening outcome, such as the effect of the ambient condition on skin temperature (thermal noise).

1.2 Research Problem

Several studies were conducted to improve the accuracy of infrared thermography in fever screening with respect to temperature measurement precision and automatic face region recognition. However during mass screening for fever in public places, it is very likely that the observation field of the camera will include several radiating objects whose temperatures are in the range of human fever. This might lead to increase in false alarm rates during automatic fever screening or when the system is operated by an inexperienced user. It is important to address this issue in order to improve the reliability and the robustness of the system with respect to perturbations and various scenarios, and to increase the efficiency (in terms of subjects scrutinized in a given time interval) of infrared thermography in mass screening of fever. This thesis focuses on identifying face regions and discriminating those with fever from other hyperthermic areas within the infrared images.

1.3 Thesis objectives

The main objective of this study is to develop and test an algorithm to address the following problems:

1. Filtering out objects with temperatures below (37^{O}C) using temperature thresholding and morphological processing.
2. Discriminate between the face and non face regions in the infrared images using template matching and hypothesis testing.

1.4 Thesis contributions

The following are the main research contributions of this thesis corresponding to the objectives above:

1. An algorithm is developed to identify the possible face regions with fever temperatures in infrared images. The algorithm includes temperature thresholding, template matching using gradient descent method, and a decision making process implemented in the framework of Neyman-Pearson hypothesis testing.
2. The algorithm is illustrated by identifying humans with fever in simulated thermal images, and in experimental images acquired with an infrared camera. False alarm

and detection frequencies of the proposed algorithm in the case of simulated images are calculated. The matching between theoretical prediction of false detection rate and actual frequency of false detections is investigated.

1.5 Organization of the thesis

Chapter 2 provides an overview of the state of the art of infrared thermography and its use in fever screening, its limitations and previous works.

Chapter 3 includes a brief review of the theoretical foundations of the functioning principles of infrared cameras and a simulation study to reproduce relevant scenarios for the current study.

Chapter 4 presents the algorithm for identifying face regions with fever temperature in infrared images; it includes image processing techniques, template matching and hypothesis testing in the Neyman-Pearson framework.

Chapter 5 presents results and illustration of the algorithm developed in chapter 4 using simulated and experimental images.

Chapter 6 summarizes the work.

CHAPTER 2

2 Background and Literature review

2.1 Thermal imaging system

With the discovery of the infrared radiation by Herschel in the early nineteenth century, related applications became major technological products. Different ways to measure the radiations lead to the development of infrared systems [5]. In the late 1950s, Texas instruments developed single element detectors that scanned scenes and produced line images. Since then infrared cameras have been extensively used in different applications.

2.1.1 Thermal imaging system theory

All objects with finite absolute temperature emit energy in the form of electromagnetic radiation, which is distributed with respect to the wavelength or the frequency within the electromagnetic spectrum [6]. The electromagnetic spectrum can be subdivided into different regions depending on their wavelength, ranging from ultraviolet, visible, infrared, and microwave. The Ultraviolet region occupies the wavelength from 0.1-0.4 μm while the visible region occupies the wavelength from 0.4-0.7 μm, which is the range that can be detected by the human eye. Bounded by the visible and microwave region is the infrared region, which occupies the wavelength from approximately 0.7-1000 microns (μm).Since all heated objects radiate in the infrared range, the terms heat and infrared radiation are often used interchangeably [6]. Infrared spectrum is in turn divided into five regions: the shortwave infrared region from 0.7-3 μm, mid wave infrared region from 3-5 μm, long wave infrared region from 8-14 μm, and the Far/Extreme IR regions from 14-1000 μm [7]. Infrared cameras used in fever screening work in the range of long wave infrared region [3]. The corresponding spectral regions are schematized in Figure 2.1[5].

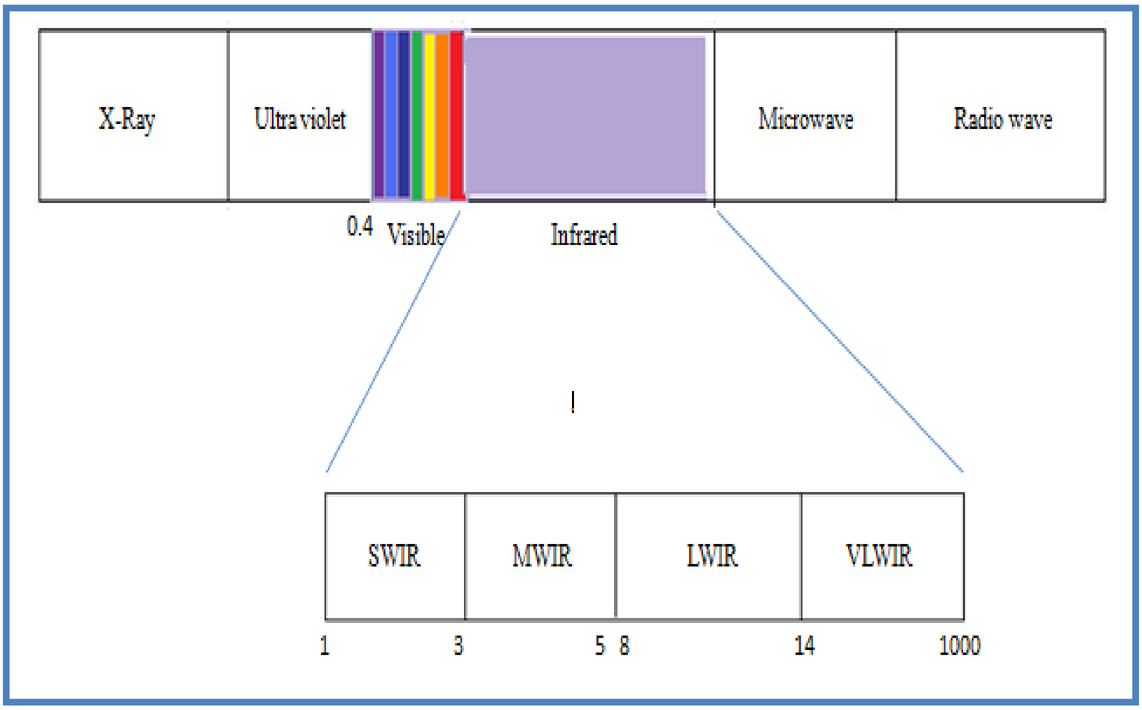

Figure 2.1: Infrared range and their location in the electromagnetic spectrum. (Reproduced from [4])

Thermal imaging devices are a combination of optics, detectors and a signal processing unit, and detect the emitted thermal energy of the target and the background present within the field of interest. The process of construction of thermal maps by thermal imaging devices can be summarized as follows [8]:

1. An optical lens collects, spectrally filters and focuses the infrared radiations received from the field of view onto a multi-element detector array.
2. Incident radiation heats the surface of the detector, which affects a property of the detector material such as electrical conductivity, which in turn translates into variation of the output signal.
3. The output signal from the detectors is then sent to a signal processing unit, which then converts it into data for display.

4. The data obtained from the signal processing unit is displayed with different colors depending on the intensity of the infrared emission. Figure 2.2, shows the basic components of the thermal imaging system.

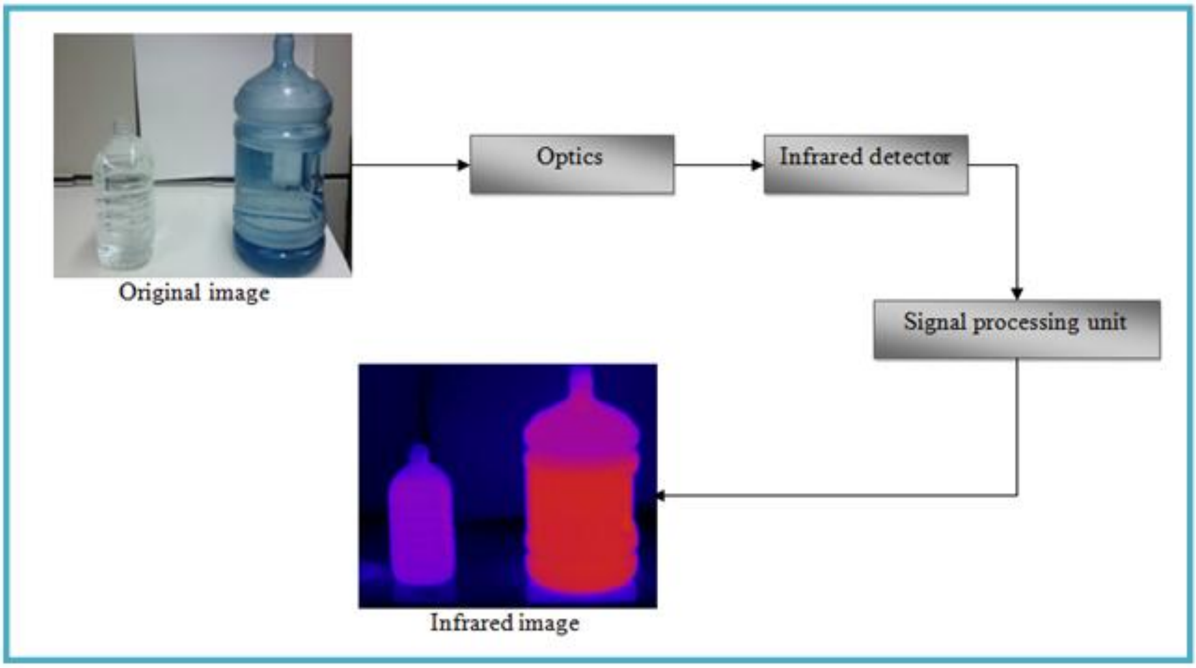

Figure 2.2: The basic components of the thermal imaging system.

2.1.2 Thermal imaging in fever screening

The outbreak of severe acute respiratory syndrome (SARS) in 2003 has infected 8437 people worldwide leading to the death of 813 people. SARS is a highly infectious disease caused by virus named corona. The cardinal symptom of SARS and other flu's is fever which is a pandemic [9] [10] [11]. Early detection of fever as a result of SARS in crowded places like airports, hospitals and major public places would prevent it from spreading. Screening of fever using invasive methods would provide accurate results but it would be very time consuming and also labour-intensive. Moreover, time constraints in places such as check in points in airports do not allow for this solution to be implemented. In order to overcome this problem the ideal device should be fast, non-invasive and also involve minimum labour. This suggests the use of infrared thermography [4]. The first infrared fever screening system was introduced by Singapore's defence science and technology agency (DSTA) and Singapore technologies electronics in 2003, during the outbreak of SARS.

2.2 Human body temperature

Temperature of the blood in the heart and the brain is generally considered as the core or internal body temperature [12]. Humans regulate and maintain a constant body temperature by exchanging heat with the environment using a variety of regulatory mechanisms, which include radiation, conduction, convection and evaporation. Infrared screening systems use the radiation emitted to estimate the temperature. Human body sites like rectal, oral ear, auxiliary and skin (in the head and neck region) which are exposed to the outer atmosphere are considered as proxies for the core body temperatures. Average temperatures for different body sites of a fever person are: rectal (37.9^{O}C), ear ($>38^{O}$C), skin (37.7^{O}C) and auxiliary (38.2^{O}C) [48]. Most of the fever screening procedures available today assumed the facial regions to be the most representative of the core body temperature, since the facial skin is thin with blood vessels close to the skin surface [12].

2.3 Types of thermal imaging systems

Thermal imaging systems available today for mass screening of fever are classified into four different types [13]:

1. Thermal imaging system type one

   Type one thermal imaging system is comprised of a thermal imager and a thermal reference source. This type of systems does not have any temperature indication but a thermal reference source, which is set at a pre-determined threshold temperature. The principle of measurement using type one systems is based on sensing the radiance difference between a person and the temperature reference source. The screened person is classified to be having fever or not based on the threshold temperature set in temperature reference source.

Examples of thermal images taken by type one thermal imaging systems are shown in Figure **2.3**.

Figure 2.3: Thermal images taken by type one thermal imaging systems using a square shaped temperature reference source, image on the left shows a person with normal temperature and image on the right is a person with fever [13].

2. Thermal imaging system type two

   This type of thermal imaging systems indicates the temperature of selected pixel (or group of pixels) within the image without using any external temperature reference system. A threshold value is represented by the set constant temperature [13]. The user can set a constant colour scale for a desired threshold temperature. This means that when a person's facial skin temperature is above the threshold temperature, the persons facial image would show the colour which is defined by the user and produces an alarm signal [13]. Examples of thermal images taken by type two systems are shown in Figure 2.4a.

3. Thermal imaging system type three

   Type three systems are similar to type one except that they have two external temperature reference sources configured with temperatures several degrees apart, where type one has only one temperature reference source. Before screening for fever, these thermal imaging systems are calibrated with the two reference temperatures. Regular change in environmental conditions is one of the major disadvantages using type three thermal imaging system, which may influence the temperature of the reference sources away from manufacturer's specifications and introduce a measurement error. Examples of thermal images taken by thermal imaging system type three is shown in Figure 2.4b.

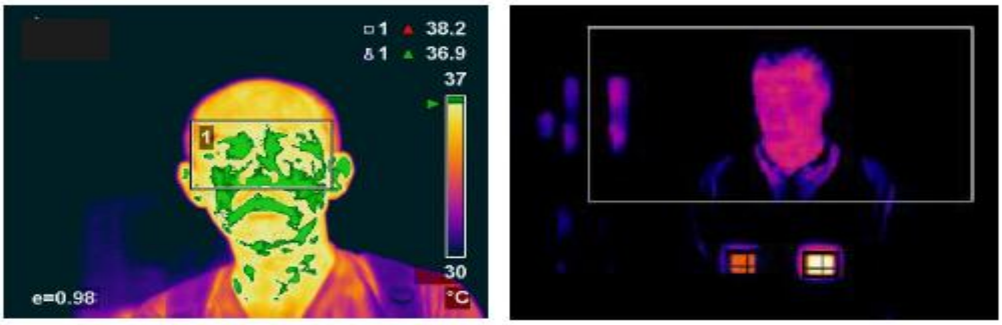

a b

Figure 2.4: (a) Thermal image of a fever person taken by type two thermal imaging system. (b) Thermal image of a normal person taken by type three thermal imaging system with two reference temperatures [13].

4. Thermal imaging system type four

Type four thermal imaging systems operate in a similar way as the type one, except that a temporal thermometer is used in addition to the thermal imager and temperature reference source. The temperature indication with this type of system is based on the temporal thermometer, which measures the temperature of the temporal artery (on the side of head). By measuring temperatures of both the subject (using temporal thermometer) and the temperature reference source at the same time, software packages then determine the difference between the temperatures and notify the operating personnel of a fever. Example of thermal image taken by type four thermal imaging systems is shown in Figure 2.5.

One of the disadvantages using type 4 systems is that they are time consuming, since they require temperatures measured by temporal thermometer in addition to the thermal imager.

Figure 2.5: Thermal image of a person taken by type four thermal imaging system with core body temperature indication [13].

2.4 Process of fever screening

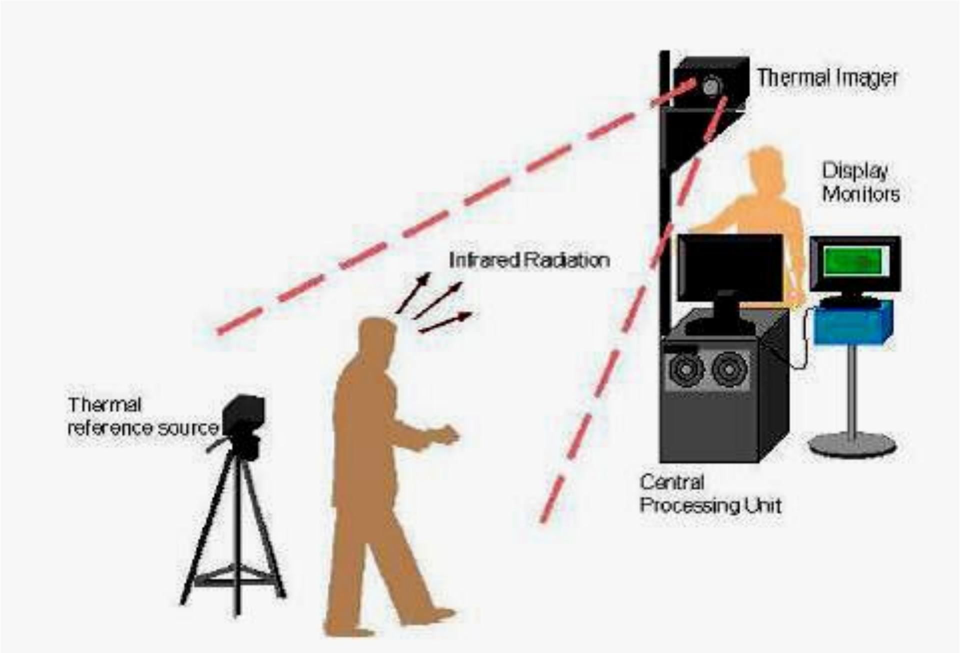

Figure 2.6: Infrared fever screening system setup [12]

Figure 2.6 shows the process of fever screening using thermal imaging system (type one), which we use further in this thesis. In the process of fever screening often adopted in airports and hospitals a stream of people are asked to walk in a predetermined path past the temperature reference source, while an operator monitors the display, as depicted in Figure 2.6. Thermal imager is pre adjusted such that it focuses only on the face regions and the temperature reference source. The radiation energy captured by the thermal imager is continuously processed by the CPU and displayed on the monitor. The processor maps the temperature into a colour scale [12]. Usually the displayed colours represent the relative increase of temperature in the following sequence: black, blue, green, yellow, and red. The operator monitoring the display then decides if the subject needs further scrutiny based on the percentage and size of the red patches on the face regions.

2.5 Parameters that characterize thermal scanners

There are several parameters that should be considered to ensure accuracy and statistically significant thermal scanner results [4]. The parameters to be considered include thermal drift, minimum detectable temperature difference, non uniformity, distance effects, error and stability of the temperature reading, spatial resolution, different environmental requirements and subject conditions [4].

Thermal drift

This class of problems is usually faced in type two thermal imagers, where the detector used in these systems tends to drift over a very short period of time and requires a regular self correction to compensate for the drift. Drift here is defined as the change in temperature during the time interval between self-corrections (i.e. variance from the true temperature) [4]. Hence minimizing thermal drift is a primary goal when considering type two scanners [14].

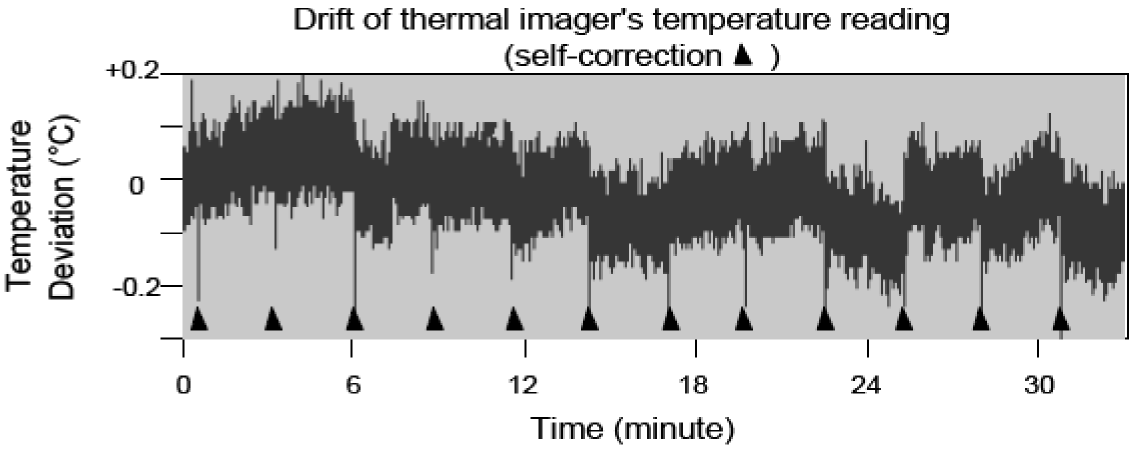

Figure 2.7: An example of the drift of a thermal imager's temperature readings between self corrections [11].

Minimum detectable temperature difference

The minimum detectable temperature difference is the smallest temperature change that a thermal imaging system is able to detect and represent by a color change, and it reflects the sensitivity in terms of the capability of the system to distinguish between two close temperature values [4]. Thermal imaging systems currently available usually are characterized by a minimum detectable temperature difference values ranging from $0.08^{O}C$ – $0.7^{O}C$. This can affect the screening process since for example a device characterized by system with temperature difference of $0.5^{O}C$ used in fever screening with a threshold temperature of $37^{O}C$, might not detect the fever person with $37.5^{O}C$.

Calibration/stability of threshold temperature

The threshold temperature is a reference that is used by the thermal imaging system to differentiate an elevated temperature from an average temperature. To ensure an accurate screening the temperature threshold should be consistent throughout the operation [10]. To determine the stability of the temperature threshold, its location in the target plane must be considered and also the thermal imagers should be calibrated with respect to the threshold temperature prior to the screening process.

All the parameters discussed have a significant affect in the thermal scanning process. By knowing the type of thermal imaging system and other factors like environmental conditions and distance between camera and subject, the influence of these parameters can be minimized to some extent [4].

2.6 Evaluating the effectiveness of infrared thermography in fever screening

Initial use of infrared thermography for screening of fever resulted in large number of false detections due to lack of experimental data [11]. Several studies were then conducted to evaluate the effectiveness of infrared thermography in fever screening [10] [11] [14] [15]. In particular studies were conducted to find the flowing:

- Best threshold temperature (to discriminate between fever and normal person)
- Spot in human body at which the skin temperature best correlates with the core body temperature.

One of the concerns in fever screening is to fix the threshold temperature (to discriminate between fever and normal person) in the case of type one Thermal imaging systems. This problem was investigated in [11] where the temperature data obtained under controlled environmental conditions was analyzed using biostatistics method, regression analysis and neural network based classification. By setting a threshold temperature of 36.2^{O}C, fever identification was achieved at an accuracy rate of 96%, with 96% sensitivity and 85.6% specificity [11]. However, these experiments were conducted by screening for one person at a time and under controlled environmental conditions.

The location of the best spot in human body at which the skin temperature best correlates with the core body temperature was studied in [10]. Temperature data obtained from the face region at different distances from the camera under controlled environmental conditions was compared with the temperature data obtained using conventional thermometers. It is estimated that the infrared thermography readings from the sides of face especially from ear at 0.5m yielded most reliable, precise and consistent estimates of conventionally determined body temperatures [10].

2.6.1 Fever screening softwares

As discussed in section (2.4) thermal imaging systems work by assigning pseudo colours to the objects in the image based on their temperatures [4]. This process is in some cases done within the camera or may be carried out through an on- or off- line computer [2]. Some of the infrared cameras available today for fever screening, as for example infrared fever screening systems, FLIR and Optotherm Thermoscreen usually are equipped with image processing software [16]. Optotherm Thermoscreen equipped with a software system used in mass fever screening is shown in Figure 2.8.

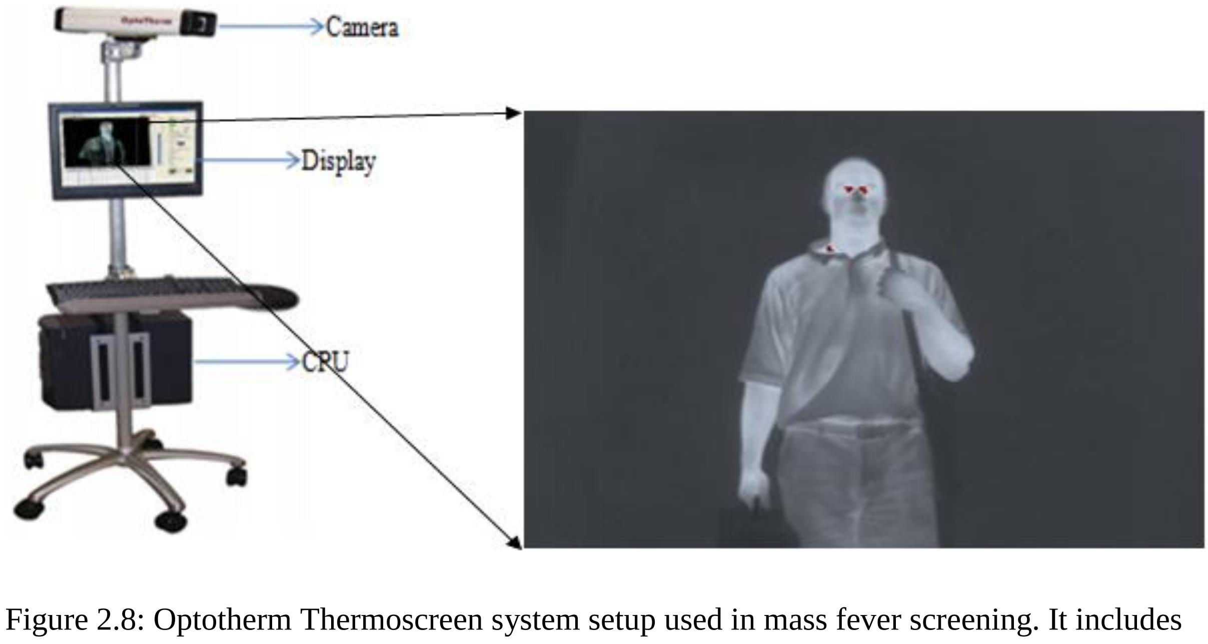

Figure 2.8: Optotherm Thermoscreen system setup used in mass fever screening. It includes infrared camera, display and a CPU [17].

Fever screening setup using FLIR A320 is shown in Figure 2.9.

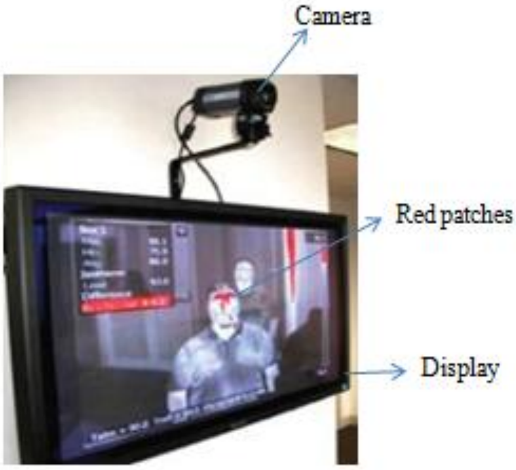

Figure 2.9: FLIR thermal imaging setup used in mass fever screening [18].

The aforementioned software packages are equipped with the following features:

- A predefined threshold temperature can be assigned such that the body temperatures above are displayed as red patches, as shown in Figure 2.9.
- An alarm sound to notify the operator if a temperature limit violation is occurred.
- Automatic screening mode with audible comments. (to reduce demand on operators)

These approaches, however, require subjects to be screened to stay in line and temperature screening to be performed for one person at a time with few seconds of interval under controlled environmental conditions. In the case of mass screening of moving people there is a possibility of presence of hyperthermic areas other than faces, implying that the operator can easily get confused because the location of the human face and its corresponding temperature is not exactly shown in the images [19]. The violation of the controlled standard conditions requires additional investigations to assess the applicability of the method and its robustness with respect to perturbations and departures from ideal conditions.

2.7 Improving the efficacy of infrared thermography in mass screening of moving people

Temperature measurement precision and system automation can greatly improve the effectiveness of infrared thermography in mass screening of moving people [20]. Automation here is intended as the capability of autonomously locating human faces in infrared images. If the device can work in an automatic way the effect of the radiating heat sources in fever screening can be found [20]. The location of human faces in infrared images is considered as a primary factor to be addressed in order to improve the efficacy of infrared thermography in mass screening of moving people for severe accurate respiratory syndrome identification.

'Pixel to temperature' is the standard process in infrared cameras (i.e. higher the temperature, the higher is the intensity associated with the pixels). In this case the location of face regions in the infrared images can be identified using simple image processing techniques such as temperature thresholding (30-42^{O}C) and morphological processing (a technique used for extracting desired image components) [21][22][19].

Identifying face regions in infrared images using neural networks and supervised learning is presented in [23]. Averaged temperature data (pixel values) of the face regions and the shape factor values are used as input data for the neural networks and supervised classification to identify the face regions. In another study [24] a multiclass multi feature fuzzy connectedness and spatial filtering using Gabor and Bessel functions are used to segment the face regions and to obtain the wavelet coefficients. A priori probability is built based on the coefficients of different facial regions which were then used for hypothesis testing. Bayesian based hypothesis testing is used to find the exact face regions [25].

Automatic face recognition in infrared images during fever screening is studied using image processing algorithms like temperature thresholding [19] and using smart biometrics system [20]. Two major problems of using infrared camera in fever screening, temperature measurement precision and automatic ability are addressed [19] [20]. Support vector machine and pattern recognition methods are used to detect face regions in infrared images. Face regions selected manually with a scale ratio of 20 by 20 are used as training vectors for the support vector machine method [20]. A false negative rate (faces not detected) of 3.73% was achieved through this method. The experimental conditions of this study did not completely embody the temperature differentiation between fever and normal faces and the presence of other hyperthermic.

In this thesis we use a combination of image processing, template matching and hypothesis testing to detect the face regions with fever temperatures.

2.8 Template matching

Template matching is a technique used in signal processing for finding small parts of an image that match a template image [26]. It is a very commonly used technique in many fields such as face detection [27], biophysical data processing [28], and photogrammetric and remote sensing [29], among others. Two main approaches have been developed: feature and image based matching.

2.8.1 Image based matching

Image based matching is used when the features in the images are not fully distinguishable or when the bulk of the template image constitutes the matching image [26]. In this case, a template is scanned over the test image in a pixel by pixel basis and meanwhile computing the correlation between them [29]. The template is confirmed to be or to be not a match with the test image based on the final correlation score. However, due to its computational complexity, image based matching is not extensively used in face recognition [29].

2.8.2 Feature based matching

In this case features of the template and test images such as edges or contours are used as the primary match measuring metrics to find the best matching location of the template in the test image [47]. While developing an automatic image retrieval system, the system should be designed in such a way that it is able to search a database of images that contain objects with similar characteristics specified by the user [30]. One idea developed by Yuille, Cohen and Hallian [45] was to represent the target object by a deformable template, that is a template model and a set of admissible geometric deformations that represent the characteristics of a target based on a priori knowledge [31].

2.9 Deformable templates

Deformable templates are comprised of a prototype and a set of admissible deformations that map it to an object that reproduce salient characteristics of a target to be matched [32]. The set of deformations is often described by an affine map. The matching between the template and the target is measured by a distance function (metric) [33]. Minimization of the distance function corresponds to the maximum similarity between the template and the test image [34]. Deformable templates with affine transformations are formally equivalent to deformable continua modelled within first gradient theory [35]. The advantages of considering deformable templates for geometric identification of facial regions are [46]:

1. Deformed templates are created with a priori knowledge about the feature in the test image to be detected.
2. Since they involve only a small number of parameters, deformable templates can be implemented easily to give a compact description of the feature in test image.

2.10 Summary

The intension of this thesis is to develop an algorithm to achieve automatic identification of fever subjects. In the process of achieving the goal, several image processing techniques were implemented along with template matching process based on gradient descent method and the Neyman-Pearson criterion based hypothesis testing were used. A real time implementation of the overall approach is not done in this thesis, however the algorithm was tested on several simulated and experimental images which represent several relevant scenarios characterizing crowded places.

CHAPTER 3

3 Radiometry review and simulation study

This chapter presents a brief review of the theoretical foundations of the functioning principles of infrared cameras and simulation study to reproduce relevant scenarios for the current study.

3.1 Radiometric quantities

One of the significant properties of the electromagnetic waves is that they can transport energy (Q) (J) [36]. The energy per unit time (dQ/dt) is called radiant flux (φ) (W). As we are concerned mainly in the distribution of power in terms of area or direction for the radiometric calculations, radiance best describes such quantity. Radiance (L) is the power per unit area and per unit solid angle (W/m^2sr) [36].

$$L(\lambda,\theta,\varphi)=\frac{\varphi}{A_s\cos\theta_s\Omega_d\lambda} \tag{3.1}$$

where

$$d\Omega_d = dA_d\cos\theta_d / R^2 \tag{3.2}$$

In equation (3.2) dA_s, dA_d are the differential areas of the source and the detector, θ_s and θ_d are angle between the normal and the line connecting both source and the detector. R is the distance between source and the detector. Figure 3.1 shows the angle between the normal and the line connecting both surface and the detector and also the distance between them.

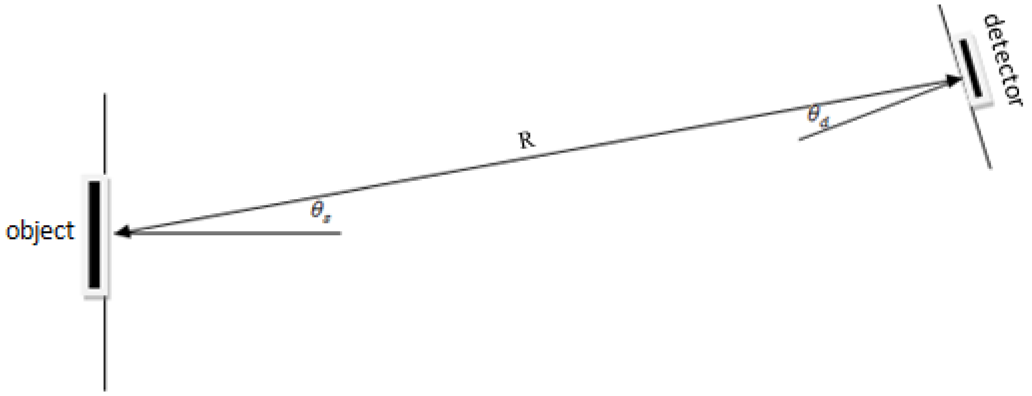

Figure 3.1: Angles and distance between the object and detector (reproduced from [37])

Rearranging equation (3.1) to solve for the radiant flux $d^2\varphi$ we get

$$d^2\varphi = \frac{L\cos\theta_s \cos\theta_d dA_s dA_d}{R^2} \tag{3.3}$$

Equation (3.3) gives the radiant flux that is leaving the differential surface of area and reaching differential area of target with angles θ_s andθ_d. In order to obtain the flux radiating from the whole surface area and reaching area of the detector, equation (3.3) is integrated over the whole range of the source and the detector.

$$\varphi = \frac{1}{R^2}\int_{A_s}\int_{A_d} L\ cos\theta_s \cos\theta_d dA_s dA_d \tag{3.4}$$

As shown in equation (3.4) the power received from the source by the detector is proportional only to $cos\theta_s, cos\theta_d$ and the square of the distance R^2 between source and the detector.

3.1.1 Planck’s radiation law

The distribution of emitted energy as a function of wavelength for a given temperature is described by Planck’s law [5]. The spectral radiance emitted by a black body per unit surface and per unit solid angle is given by

$$L_{\lambda,b}(\lambda,T)=\frac{2hc^2}{\lambda^5[\exp\left(\frac{hc}{\lambda KT}\right)-1]} \qquad (3.5)$$

where the unit for the blackbody spectral radiance is given by$(W/m^2 sr\ \mu m)$, using the first and second radiation constants the equation (3.5) can be rewritten as

$$L_{\lambda,b}(\lambda,T)=\frac{c_1}{\lambda^5[\exp\left(\frac{c_2}{\lambda T}\right)-1]} \qquad (3.6)$$

Planck's radiation curve for black bodies at different temperatures is shown in Figure 3.2.

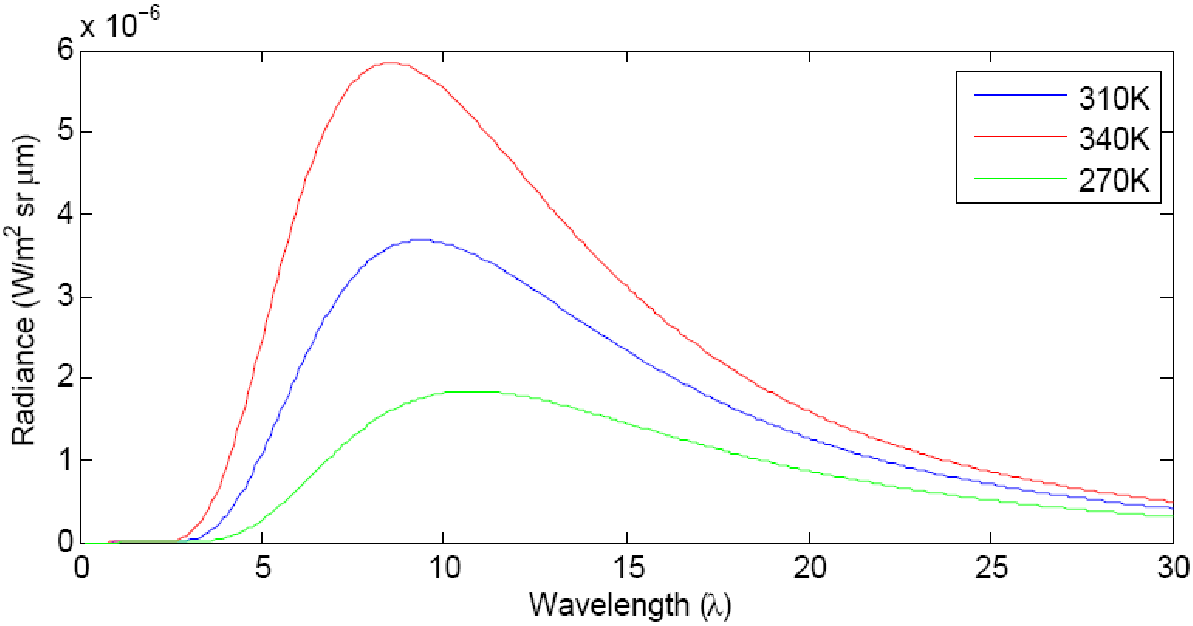

Figure 3.2: Spectral radiance curve of black body at temperatures 270K (green), 310K (blue) and 340K (red).

From equation (3.6) it is clear that the object with higher temperatures has high radiance values. Integrating equation (3.6) over all wavelengths gives the total exitance from a black body, which is given in equation (3.7)

$$L_b=\int_0^\infty \frac{c_1}{\lambda^5[\exp\left(\frac{c_2}{\lambda T}\right)-1]} \qquad (3.7)$$

Equation (3.7) is the radiance exitance from the black body only and in case of real sources the above equations must be corrected [5]. The correction factor to be used is the emissivity (ε), which is discussed briefly in the following section.

3.1.2 Emissivity (ε)

Emissivity is the property of a surface to emit energy. It is given by ratio of the radiation emitted by a surface to the radiation emitted by a black body under same conditions of temperature, direction and spectral band of interest [46]. Because it is a ratio the value of emissivity can only be within the range of 0.0 to 1.0 [38]. The directional spectral emissivity of a surface at temperature T, which is emitting in direction (θ, φ) is given by [5]

$$\varepsilon(T,\theta,\varphi) = \frac{L_\lambda(\lambda,T,\theta,\varphi)}{L_{\lambda,b}(\lambda,T)} \tag{3.8}$$

In our case we assumed emissivity is dependent only on the temperature and the spectral exitance curve of the black body is scaled by the emissivity to give the gray body spectral exitance curve.

$$L_\lambda(\lambda,T) = \varepsilon(T) L_{\lambda,b}(\lambda,T) \tag{3.9}$$

Substituting the black body spectral radiance from equation (3.9) we get

$$L_\lambda(\lambda,T) = \int_0^\infty \varepsilon(\lambda,T) \frac{c_1}{\lambda^5[\exp\left(\frac{c_2}{\lambda T}\right)-1]} d\lambda \tag{3.10}$$

Spectral radiance curve for a real source with temperature 310K at two different emissivities is shown in Figure 3.3.

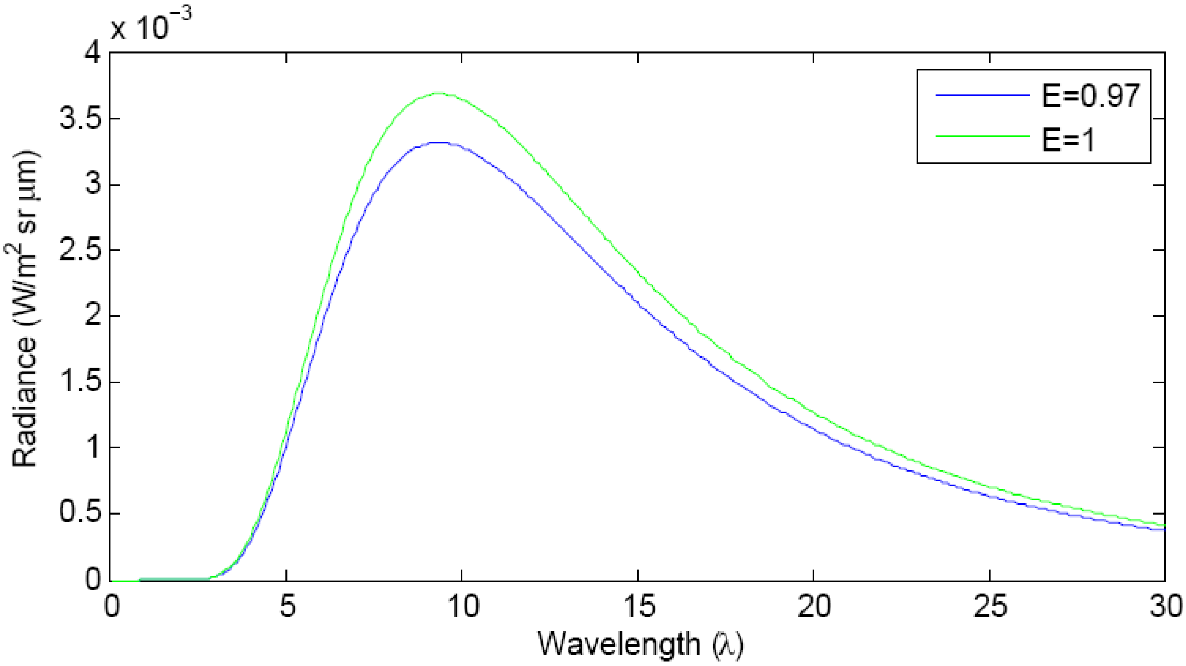

Figure 3.3: Spectral radiance curve of a real source with temperature (310K) at two different emissivities.

where the infrared cameras work at wavelength range of 8-12μm, equation (3.10) was integrated only within the range of 8-12μm. In this case equation (3.10) was integrated with in the wavelength range of 8-12μm.

$$L_\lambda(\lambda,T)=\int_{8}^{12}\varepsilon(\lambda,T)\frac{c_1}{\lambda^5[\exp\left(\frac{c_2}{\lambda T}\right)-1]}d\lambda \tag{3.11}$$

Equation (3.11) gives the total exitance from the surface of the source within the wavelength range of the camera. Substituting equation (3.11) to (3.4) gives the total radiant flux density $\left(\frac{W}{m^2}sr\ \mu m\right)$ that is reaching the surface of the detector.

$$\varphi=\frac{1}{R^2}\int_{A_s}\int_{A_d}L\ cos\theta_s\cos\theta_d dA_s dA_d\int_{8}^{12}\varepsilon(\lambda,T)\frac{c_1}{\lambda^5[\exp\left(\frac{c_2}{\lambda T}\right)-1]}d\lambda \tag{3.12}$$

3.2 Simulation models

Simulations were carried out to understand the interaction between different radiating objects within the image. Two models were used in the simulations, spherical and cylindrical shapes. A brief description of the model creation was discussed in the following sections.

3.2.1 Models

First model is a hemispherical shape, whose coordinates are defined as: [39]

$$x = rsin\theta cos\varphi$$

$$y = rsin\theta sin\varphi$$

$$z = rcos\theta$$

where r is radius of the sphere, θ is the inclination varied from 0 to π and φ is the azimuth angle varied from 0 to π (if varied from 0 to 2 π gives a complete sphere). The axis z is varied from 0 to r. A model of spherical coordinate system was shown in Figure 3.4.

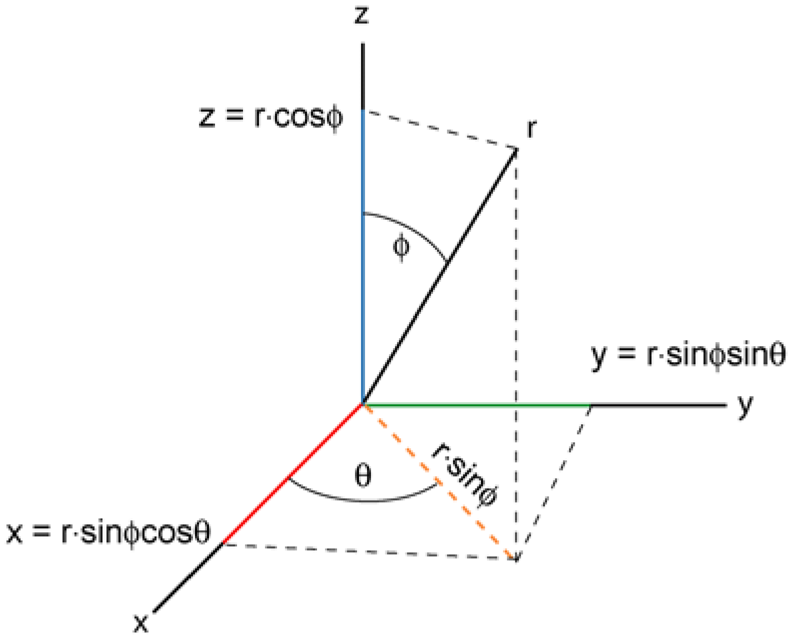

Figure 3.4: Model of spherical coordinate system.

Next model to be created is a cylinder, whose coordinates are given by

$$x = r\cos\varphi$$

$$y = r\sin\varphi$$

In this case r is the radius of the cylinder, and φ (azimuth angle) is varied from 0 to π to create half cylinder and z is height of the cylinder. A model of cylindrical coordinate system is shown in Figure 3.5.

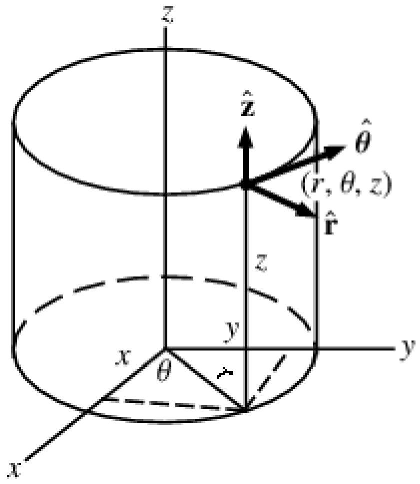

Figure 3.5: Model of cylindrical coordinate system.

As seen in Figure 3.6, surface of the target is divided into different facets and the radiation emitted from each facet is calculated in the simulations. A view of the radiation reaching the surface of the detector from the normal pointing out from each facet is shown in Figure 3.6.

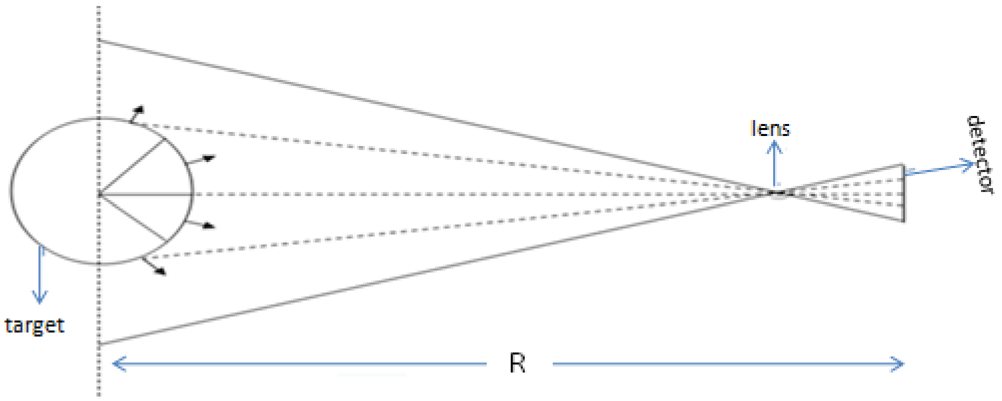

Figure 3.6: A view of simulation process.

where $\theta_1$and θ_2 are angles between the normal to the surfaces of source and detector to the line connecting them, R is the distance between surface of the source and detector. The following equation refers to the radiation flux density from the surface according to the angles $\theta_1$and θ_2.

$$\varphi = \frac{1}{R^2} \int\limits_{A_s} \int\limits_{A_d} L \, cos\theta_s \cos\theta_d dA_s dA_d \int_8^{12} \varepsilon(\lambda, T) \frac{c_1}{\lambda^5 [\exp\left(\frac{c_2}{\lambda T}\right) - 1]} d\lambda \qquad (3.13)$$

where, the first term in equation (3.13) includes the angle between differential area of the detector (dA_d) to the differential area of the source (dA_s) and the distance between them (R^2), where the second term includes self emitted spectral radiance from the surface of source, for the long wave infrared region, depending on their temperatures.

3.2.2 Simulation result

Parameters (temperature and emissivity) used in the simulations are shown in Table 3.1:

Region	Temperature	Emissivity
Face (non fever)	36^{O}C	0.97
Face (fever)	37.5^{O}C	0.97
Body region	36^{O}C	0.72 (clothes)
Heat source	36-42 ^{O}C	0.7-0.95

Table 3.1: Parameters used in simulations (temperature and emissivity) for different regions.

Two different images are shown in Figure 3.7. The first one is the radiance image with a person alone and radiance image of a person in the presence of a heat source as shown in Figure 3.7b.

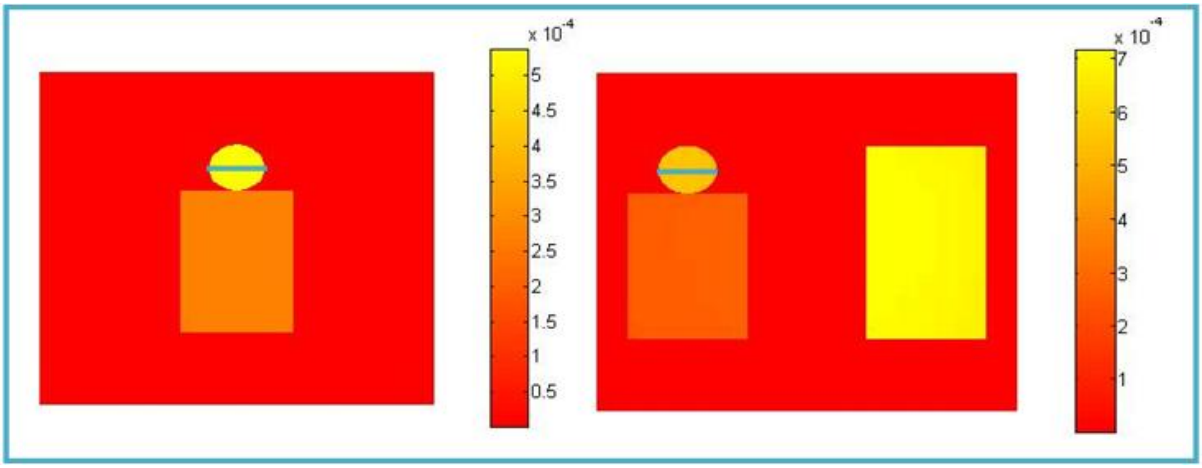

Figure 3.7: (a) Simulated image of a person with temperature (36^{O}C), (b) Simulated image of a person (36^{O}C) and a heat source (40^{O}C)

It can be observed from Figure 3.7b, that the intensity of the assumed face region is changed in the presence of heat source. A plot of the Pixel intensity at selected regions from face regions (blue line) in both images of Figure 3.7 is shown in Figure 3.8.

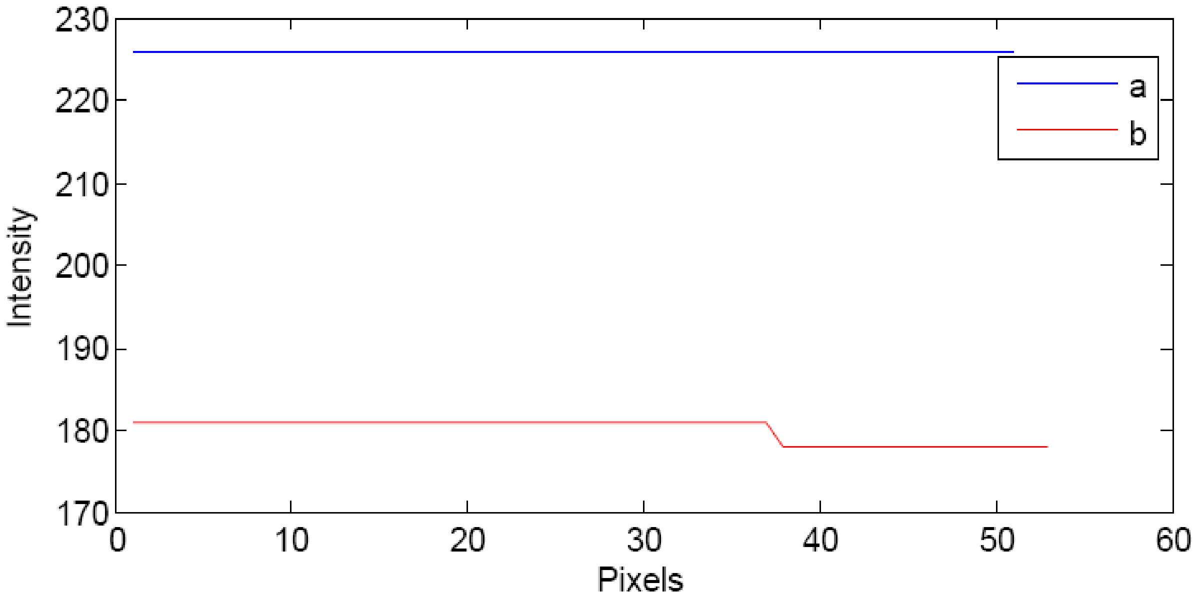

Figure 3.8: Showing the intensity of the selected pixels from figure (3-10a) (Blue) and the intensity of the selected pixels from figure (3-10b) (red)

From Figure 3.8, it is clear that the intensity of the pixel regions changes in the presence of other heat sources within the field of view of camera. In the case of thermograms without temperature values (colour scale only); it would lead to erroneous results in fever screening [8].

CHAPTER 4

4 Algorithm for identification of subjects with fever

4.1 Methodology for automatic fever person identification

This chapter describes the template matching methodology developed to identify face shapes in the infrared images. It includes object selection, template matching and decision making process. A block diagram of the algorithm for face recognition and temperature estimation based on template matching and temperature thresholding is shown in Figure 4.1.

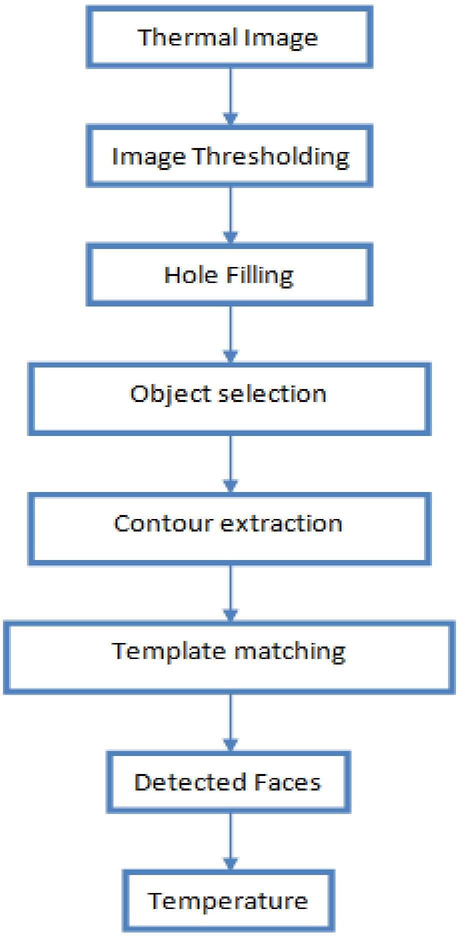

Figure 4.1: A flowchart illustrating the image processing steps implemented to locate human faces on the 2D thermal images.

In the following sections an infrared image is used to show the process up to the contour extraction step.

4.1.1 Thermal image thresholding

A temperarure reference source either internal or external is usually used by all the four types of thermal imaging systems [13]. This reference source is used as a set point to differentiate between fever and normal temperatures. An external reference source of 36.5C [11] is used as a threshold temperature in our experiments (in chapter 5). The reference source used in our experiments is shown in Figure 4.2. First step during object identification in any image is to convert it to binary image (black and white), because this step makes it easy to select the desired objects and to extract their contours [19]. In this case we used the averaged pixel values of the reference temperature in the image as a threshold to obtain a binary image (pixel values above the threshold are set to 1 and pixel values below are set to 0). Thresholding process applied to one of the images obtained by an infrared camera is as shown below:

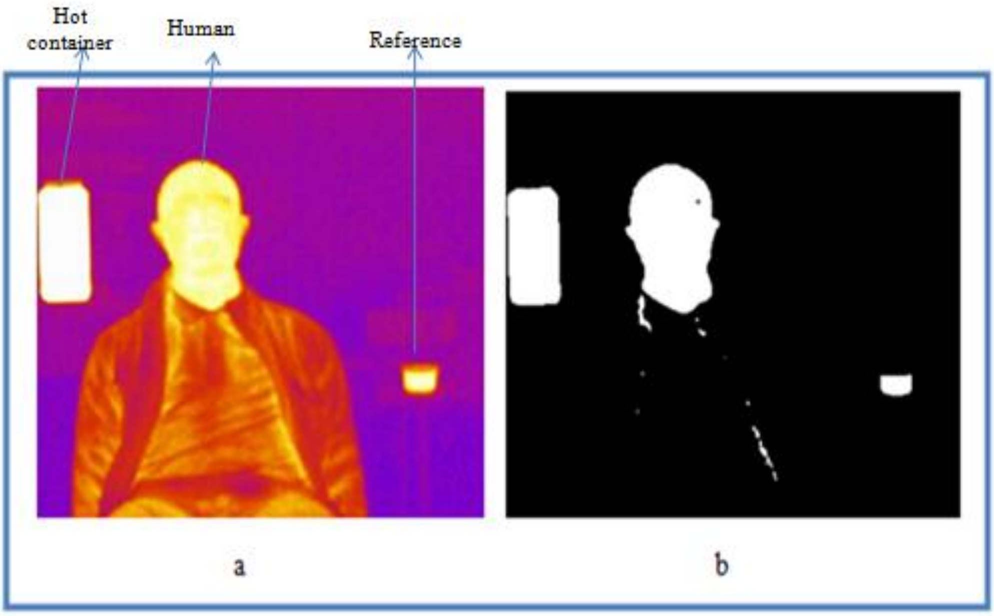

Figure 4.2: (a) An original 2D thermal image of a person and hot container (b) after applying image thresholding step.

As seen in Figure 4.2b, face region and a heat source with pixel values above the threshold were set to 1 (white). Regions such as shirt and background with the pixel values below the threshold are set to 0 (black).

4.1.2 Hole filling

The binary image obtained after temperature thresholding has few small black spots within the face region, as seen in Figure 4.3(a). The presence of black spots might affect the contour extraction step as we need the whole face region to be one object, the black spots in the face regions would be considered as holes. As we assumed a circle as a template to match the face because of the similarity with ellipses (section 4.2), the presence of additional contours (contours of small holes) might result in a wrong match. Holes in the face region are filled by converting each 0 pixel value into 1. The action is executed through the MATLAB *imfill* command with the typical result shown in Figure 4.3. Face region after filling the holes is shown in Figure 4.3b.

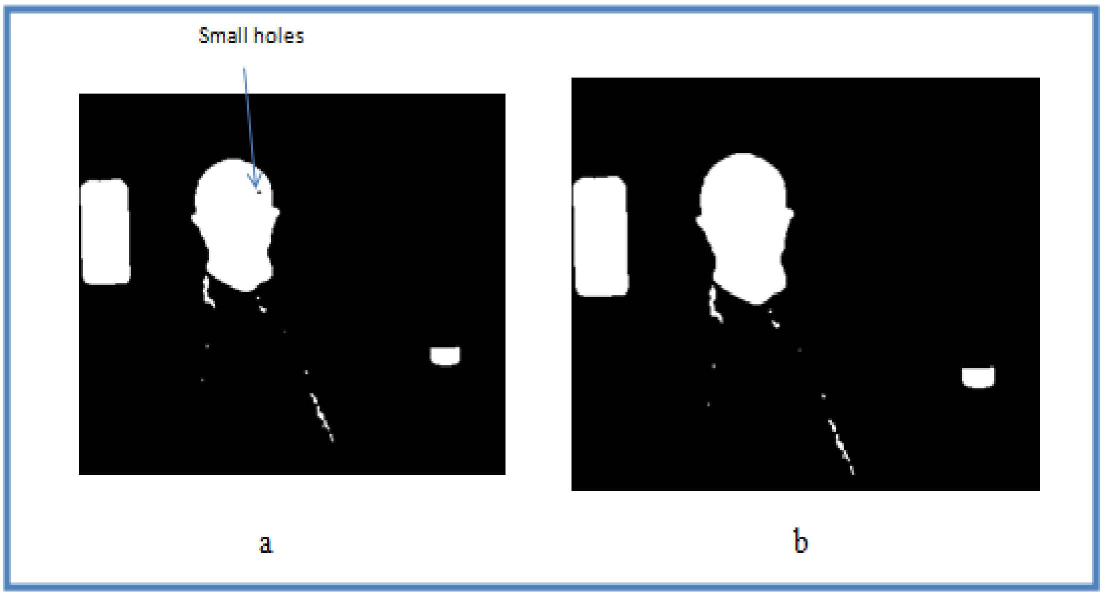

Figure 4.3: (a) Face region with small holes after applying image thresholding step. (b) Face region after applying holes filling step.

4.1.3 Object selection

It can be seen that in Figure 4.3 there are several small objects, which will affect the automation process. During automatic template matching process the presence of these small objects might lead to false results (as they are also considered as target objects). To remove these objects morphological operations can be used [19]. The MATLAB *imopen* command is used in this step. It performs morphological opening on the binary image with a structuring element chosen to a matrix of one's [50]. The morphological open operation is erosion followed by dilation. The steps erosion removes the pixels on object boundaries, whereas the step dilation adds pixels to the object boundaries based on the size of the structuring element [40]. Binary image after processing with the morphological open operation is shown in Figure 4.4b, where there are only two big objects left: face and hot container.

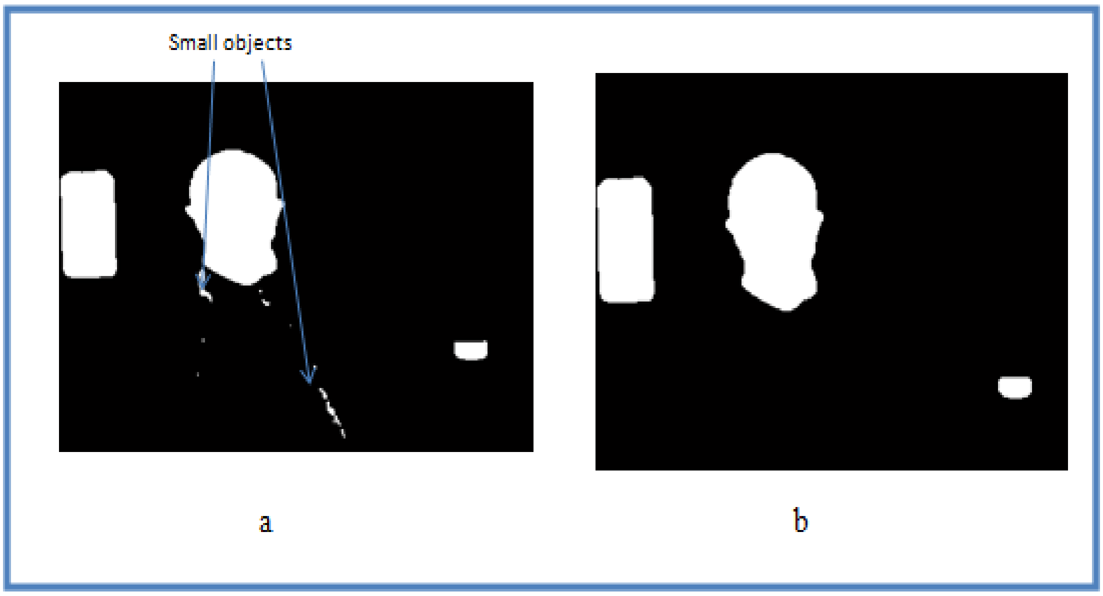

Figure 4.4: (a) The image with remaining small objects other than the face and hot container after applying hole filling step. (b) The image after applying main objects selection step.

4.1.4 Contour extraction

Final step is to extract the contours of the objects in the binary image. The MATLAB *contourc* command is used in this step. It computes the contour matrix from the matrix representing the input object. Extracted contours of the objects representing face and heat source in Figure 4.4(b) are shown in Figure 4.5.

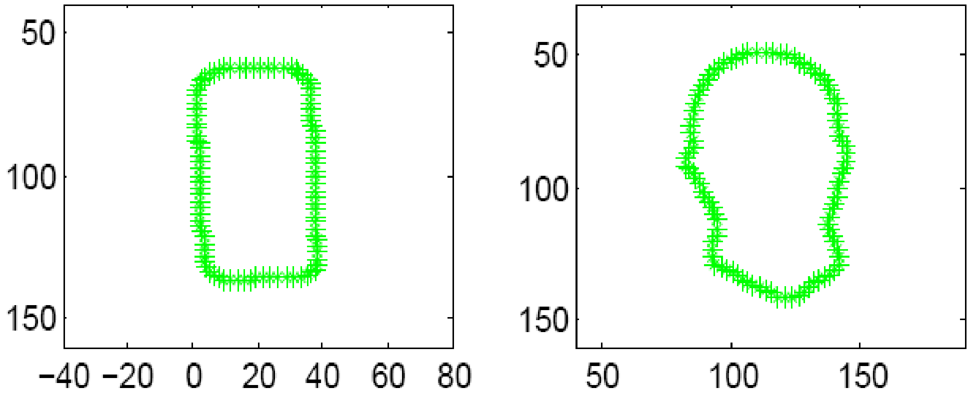

Figure 4.5: Extracted contours after object selection step (a) contour of the heat source (b) contour of the face.

4.1.4.1 Normalizing the contours

Coordinates representing the contours are normalized prior to the template matching process. This is done by dividing each coordinate by the omologous coordinate of mean of the contour that is the centroid of the set of point sampling the contour. This step is needed because the coordinates of the contours extracted from different regions of the image vary from one to another. The contours extracted from the images are then used in the next step template matching.

4.2 Shape based Template matching

Template used for matching the shapes extracted in the previous steps is a circle. The rationale behind this choice is the fact that in terms of geometry we want to distinguish face regions that are approximately oval from other radiating sources that are approximately rectangular. Since the template is deformed by an affine map, the deformed shape is an ellipse which is expected to be more similar to a typical face contour than to a reference rectangular radiator. An outline of the steps involved in template matching process is shown in Figure 4.6.

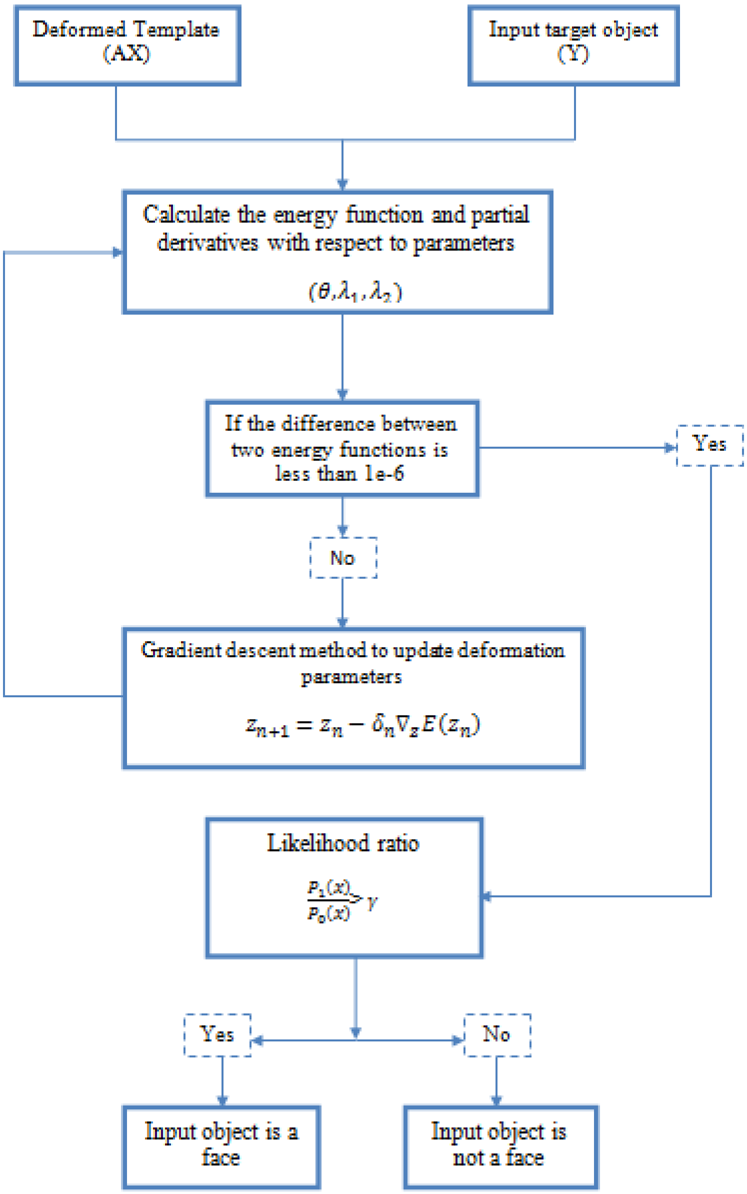

Figure 4.6: A flowchart illustrating the steps involved in the process of template matching.

Let X be a set of points x_i $(1 \leq i \leq N)$ representing coordinates of the template that is a set of samples of the contour describing the template. Similarly let Y be a set of points y_i describing the contour of the target object. The integer N refers to the number of points of the template and target objects.

Let

$$y_i = Ax_i \tag{4.1}$$

$$A = RS = \begin{bmatrix} \cos\theta & -\sin\theta \\ \sin\theta & \cos\theta \end{bmatrix} \begin{bmatrix} \lambda_1 & 0 \\ 0 & \lambda_2 \end{bmatrix}$$

where $\theta \in [0,2\pi)$ is a rotation angle and λ_1 and λ_2 are positive stretching parameters. Therefore R and S are respectively, a rotation matrix and a symmetric positive definite matrix whose combined action maps the circle (unreformed template) into an ellipse and rotates it with respect to the initial reference frame. The (2×2) matrix A is therefore non-singular since $\det A = \det R \det S = \lambda_1 \lambda_2 > 0$. This implies that the initial template cannot be mapped into a shape with null area, and therefore degenerate cases are avoided due to the properties of the mapping function.

Let

$$z = \begin{pmatrix} \theta \\ \lambda_1 \\ \lambda_2 \end{pmatrix}$$

be the collection of parameters that define the linear transformation A, and let

$$E: z \in \mathbb{R}^3 \mapsto E(z) \in \mathbb{R}^+$$

be the least square distance between the two point sets defining the deformed template and the target object

$$E = \sum_{i=1}^{N} ||y_i - Ax_i||^2 \tag{4.2}$$

The objective of the matching is to find the set of parameters z^* that minimizes $E(z)$. This corresponds to the following optimization problem

$$\boldsymbol{z^* = argmin_z E(z)}$$

(4.3)

which is equivalent to the following root searching problem

$$\nabla_z E\left(z^*\right) = 0 \tag{4.4}$$

where

$$\nabla_z := \begin{pmatrix} \frac{\partial}{\partial\theta} \\ \frac{\partial}{\partial\lambda_1} \\ \frac{\partial}{\partial\lambda_2} \end{pmatrix}$$

is the gradient, in components form, with respect to the state vector z. Expanding equation (4.2) the energy function can be rewritten as:

$$E = \sum_{i=1}^{N} \left(2y_i^T y_i + 2x_i^T A^T A x_i - (x_i^T A^T y_i + y_i^T A x_i)\right) \tag{4.5}$$

where

$$A^T A = \begin{pmatrix} \lambda_1^2 & 0 \\ 0 & \lambda_2^2 \end{pmatrix}$$

The solution of the minimization problem is found by using the gradient descent method.

4.3 Gradient descent method

Gradient descent method (steepest descent) is a root searching family of algorithms. It is based on the observation that if the real-valued function $E(z)$ is continuously differentiable in a neighbourhood of a point $\bar{z}$, then $-\nabla_z E(\bar{z})$ is the direction of steepest variation of $E(\bar{z})$ [41]. Formally, let E be a scalar valued function satisfying:

$$\text{Non negativity: } E(z) \geq 0 \ \ \forall z$$

$$\text{Lipschitz continuity of the gradient: } \exists \kappa > 0\text{: } \|\nabla_z E(z_1) - \nabla_z E(z_2)\| \leq \kappa \|z_1 - z_2\| \ \ \forall z_1, z_2$$

A key implication of the properties above is the Descent Lemma that we enunciate below. For the proof consult for example [42].

Descent Lemma [42]: Let $E(z)$ be a non negative, Lipschitz continuous scalar function. Then for every $\tilde{z}$ the following relation holds:

$$E(z + \tilde{z}) \leq E(z) + \tilde{z}^T \nabla_z E(z) + \frac{\kappa}{2} \|\tilde{z}\|^2$$

Consider the iterative algorithm (gradient descent)

$$z_{n+1} = z_n - \delta_n \nabla_z E(z_n) \tag{4.5}$$

where $\delta_n > 0$ and the integer n labels the iteration. The Descent Lemma implies the convergence of the gradient descent iterator:

Convergence of the gradient descent algorithms [42]: Consider the sequence $\{z_n\}_{n=1}^{\infty}$ generated by the gradient descent iterator in Equation (4.5). For $0 < \delta_n < 2/\kappa$ the following asymptotic convergence result holds

$$\lim_{n \to \infty} \nabla_z E(z_n) = 0$$

For the proof we remind again to [42]. In view of the convergence of the gradient descent algorithms it follows that by iteratively updating the set of parameters that define the linear transformation A according to the iterator (4.5) we find a solution of the problem (4.4) that is a minimum of the distance function E. Components of the gradient of the const function are given by

$$\frac{\partial E}{\partial z_i} = \sum_{i=1}^{N} \left(2x_i^T \frac{\partial A^T A}{\partial z_i} x_i - \left(x_i^T \frac{\partial A^T}{\partial z_i} y_i + y_i^T \frac{\partial A}{\partial z_i} x_i \right) \right)$$

where the first term in the right-hand side is zero for $z_i = \theta$.

The convergence of gradient descent algorithms determines also bounds for the updating step δ_n in terms of the Lipschitz constant κ. In this work we use the step size 0.001. Iterations are carried out until the difference between two consecutive values of the energy function is less than a pre-set tolerance (10^{-6}used here). The converged value for E is the minimized least square distance between the deformed template and the target, and the corresponding set of parameters $z^*$is the minimizer.

4.4 Decision making rule

The converged deformed template obtained from the gradient descent iterations may or may not correspond to an actual human face. In order to complete the template matching process it is necessary to decide if the converged value of the least square distance between the deformed template and the target is representative of the searched feature (human face). The decision making process is executed by introducing a binary hypothesis test in the Neyman-Pearson decision making framework.

4.4.1 Hypothesis testing

Let E be the converged value of the least square distance between a target contour and the deformed template. In order to decide if such value corresponds to a face region rather than to any other radiating object in the field of view we consider a simple binary hypothesis testing framework. We define the null and the alternative hypotheses to be respectively

$$H_0: E \text{ does not correspond to a face region}$$
$$H_1: E \text{ corresponds to a face region}$$

The hypothesis test is carried out in a probabilistic framework by building the two continuous probability density functions $p_0(E)$ and $p_1(E)$ associated respectively to H_0 and H_1 [43]. The probability density functions are determined by considering two populations $\{E\}_0$ and $\{E\}_1$ of minimum least square values associated to converged deformed templates, where the convergence is achieved on known regions that are respectively radiating sources not corresponding to face regions, and radiating sources corresponding to face regions. Infrared images [49] used to extract contours to build the two probability density functions are shown in Figure 4.7.

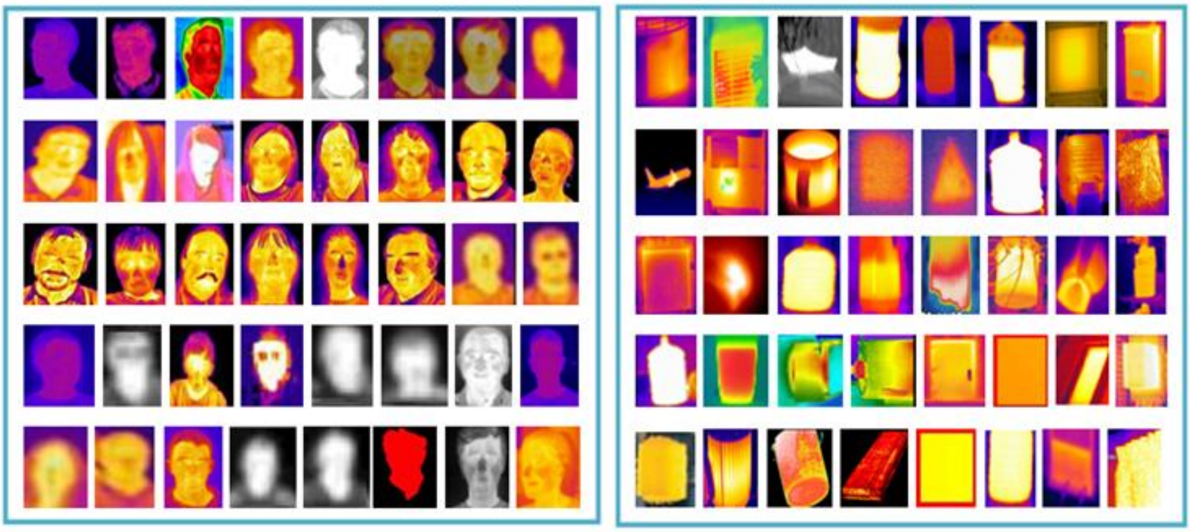

a

b

Figure 4.7: Images used in the training database. (a) Faces $\{E\}_1$ and (b) Non faces $\{E\}_0$ used as a training data for the proposed algorithm.

The cardinality of each population is 40, that is, 40 contours for each type were extracted from the infrared images. Given the populations of minimum least square distances representing the two hypotheses, the first two statistical parameters were computed for each population as

$$\mu_0 = \frac{1}{M_0}\sum_{i=1}^{M_0}\{E_i\}_0 \quad \sigma_0^2 = \frac{1}{M_0}\sum_{i=1}^{M_0}(\{E_i\}_0 - \mu_0)^2$$
$$\mu_1 = \frac{1}{M_1}\sum_{i=1}^{M_1}\{E_i\}_1 \quad \sigma_1^2 = \frac{1}{M_1}\sum_{i=1}^{M_1}(\{E_i\}_1 - \mu_1)^2$$

where μ_0 and μ_1 are the mean values of the two populations with standard deviations σ_0 and σ_1. By using these parameters the Gaussian approximations of the discrete distributions associated with the two populations are considered, with corresponding density functions given by

$$p_0(E) = \frac{1}{\sigma_0\sqrt{2\pi}}\exp\left(-\frac{1}{2}\left(\frac{E-\mu_0}{\sigma_0}\right)^2\right)$$
$$p_1(E) = \frac{1}{\sigma_1\sqrt{2\pi}}\exp\left(-\frac{1}{2}\left(\frac{E-\mu_1}{\sigma_1}\right)^2\right)$$

Plots of the discrete distributions (normalized histograms) and the corresponding Gaussian continuous approximations are shown in Figure 4.8 and Figure 4.9, and the values of the statistical moments are given in Table 4.1. With the Gaussian approximation the population of converged minimum least square distances is extended to negative values, and therefore tales of the continuous distributions belong to the region not included in the original discrete distributions.

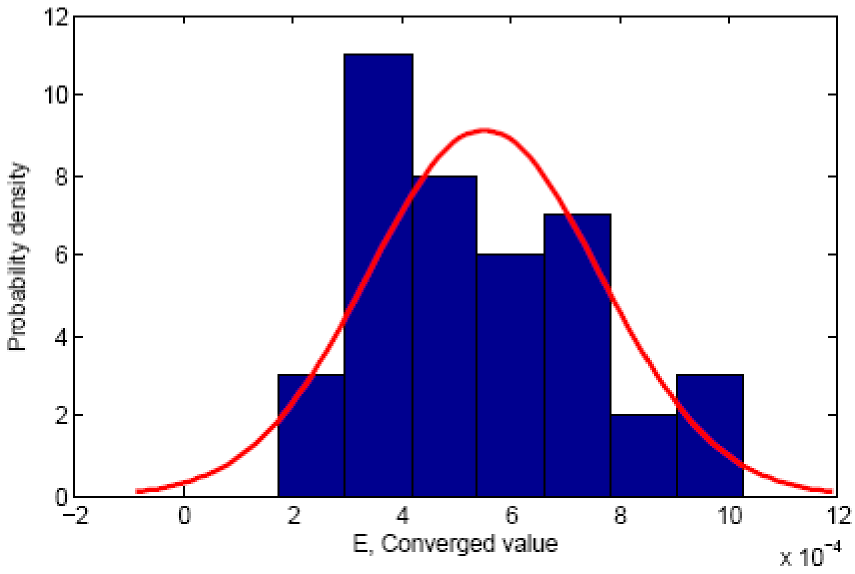

Figure 4.8: Discrete distribution and continuous Gaussian approximation for the population $\{\boldsymbol{E}\}_0$ of converged minimum least square distances for non-face regions.

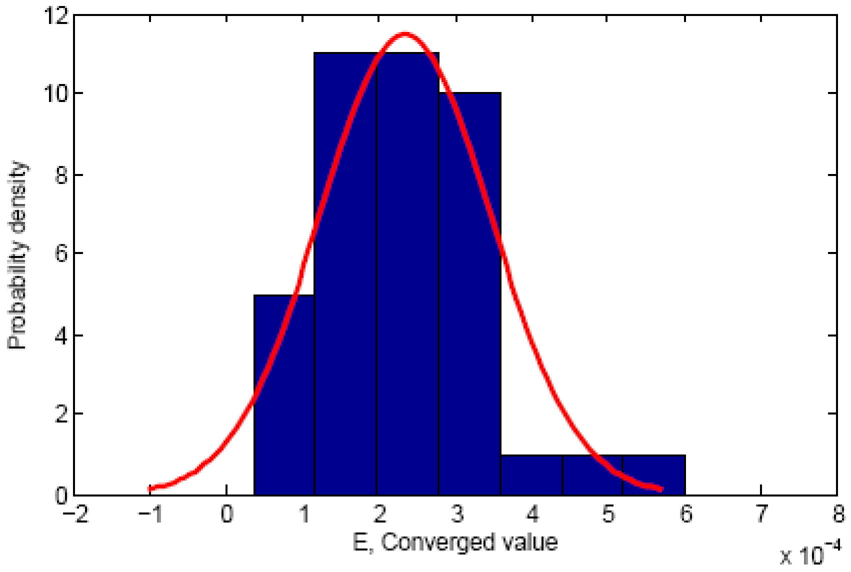

Figure 4.9: Discrete distribution and continuous Gaussian approximation for the population $\{\boldsymbol{E}\}_1$ of converged minimum least square distances for the face regions.

Parameter	μ_0	σ_0	μ_1	σ_1
Value	0.000553	0.000212	0.000234	0.000112

Table 4.1: Resulting parameters of the probability density functions $\boldsymbol{p_0}$ and $\boldsymbol{p_1}$.

The hypothesis test to select H_1 against H_0 is defined in terms of the log-likelihood ratio

$$\Lambda(E) = \ln \frac{p_1}{p_0}(E) = \left(\frac{E-\mu_0}{\sigma_0}\right)^2 - \left(\frac{E-\mu_1}{\sigma_1}\right)^2 \gtrless_{H_0}^{H_1} \gamma \tag{4.6}$$

where the threshold γ is determined by applying the Neyman-Pearson criterion as explained below.

4.4.1.1 Neyman-Pearson criterion

The threshold γ is determined by using the Neyman-Pearson criterion, which assigns the threshold value corresponding to the maximum detection probability achievable for a given false detection rate [26].

The detection region for the hypothesis H_1 is defined as the set

$$\varrho_1(E,\gamma) \coloneqq \{E\colon \Lambda(E) > \gamma\}$$

In the Neyman-Pearson framework the threshold γ is determined by imposing a constraint on the false detection rate. The probability of detection and the probability of false detection are related to the detection region by

$$P_D = \int_{\varrho_1(E,\gamma)} p_1(E)\,dE \tag{4.6}$$

$$P_F = \int_{\varrho_1(E,\gamma)} p_0(E)\,dE \tag{4.7}$$

The probability of detection and Probability of false alarm values for a certain threshold are shown in Figure 4.10.

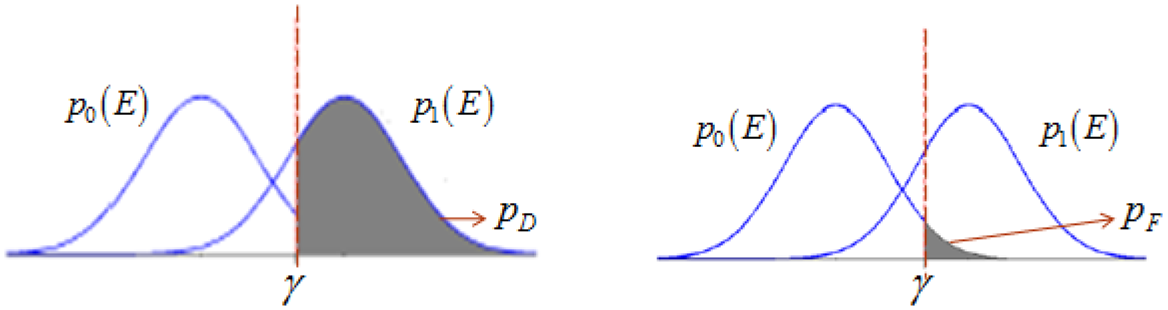

Figure 4.10: False alarm and detection values for a certain threshold.

By setting the value of P_F to the desired false detection rate the threshold is determined by iteratively solving to convergence the integral equation (4.8) for γ. By introducing the coefficients (from equation 4.6)

$$a = \frac{1}{\sigma_0^2} - \frac{1}{\sigma_1^2}$$
$$b = \frac{\mu_0}{\sigma_0^2} - \frac{\mu_1}{\sigma_1^2}$$
$$c(\gamma) = \frac{\mu_0^2}{\sigma_0^2} - \frac{\mu_1^2}{\sigma_1^2} - \gamma$$

the region of detection can be defined in terms of the roots of the quadratic equation

$$a\mathrm{E}^2 - 2bE + c(\gamma) = 0$$

with roots given by

$$E^{\pm}(\gamma) = \frac{b \pm \sqrt{b^2 - ac(\gamma)}}{a} \tag{4.8}$$

Therefore the region of detection can be written as:

$$\varrho_1(\gamma) = \begin{cases} (-\infty, E_1) \cup (E_2, \infty) & \text{if } a > 0 \\ (E^-, E^+) & \text{if } a < 0 \end{cases}$$

In our case, from the values in Table 4.1 we have $a < 0$ and therefore the relation to determine γ (probability of false alarm) is given by

$$P_F = \int_{E_1(\gamma)}^{E_2(\gamma)} p_0(E)\,dE \tag{4.9}$$

By setting the probability of false alarm constraint $P_F = 0.05$, equation (3.14) is solved using the bisection method to find γ. The corresponding converged threshold value is $\gamma = 0.0011$. Figure 4.11 shows the convergence of the bisection algorithm with tolerance (10^{-10}).

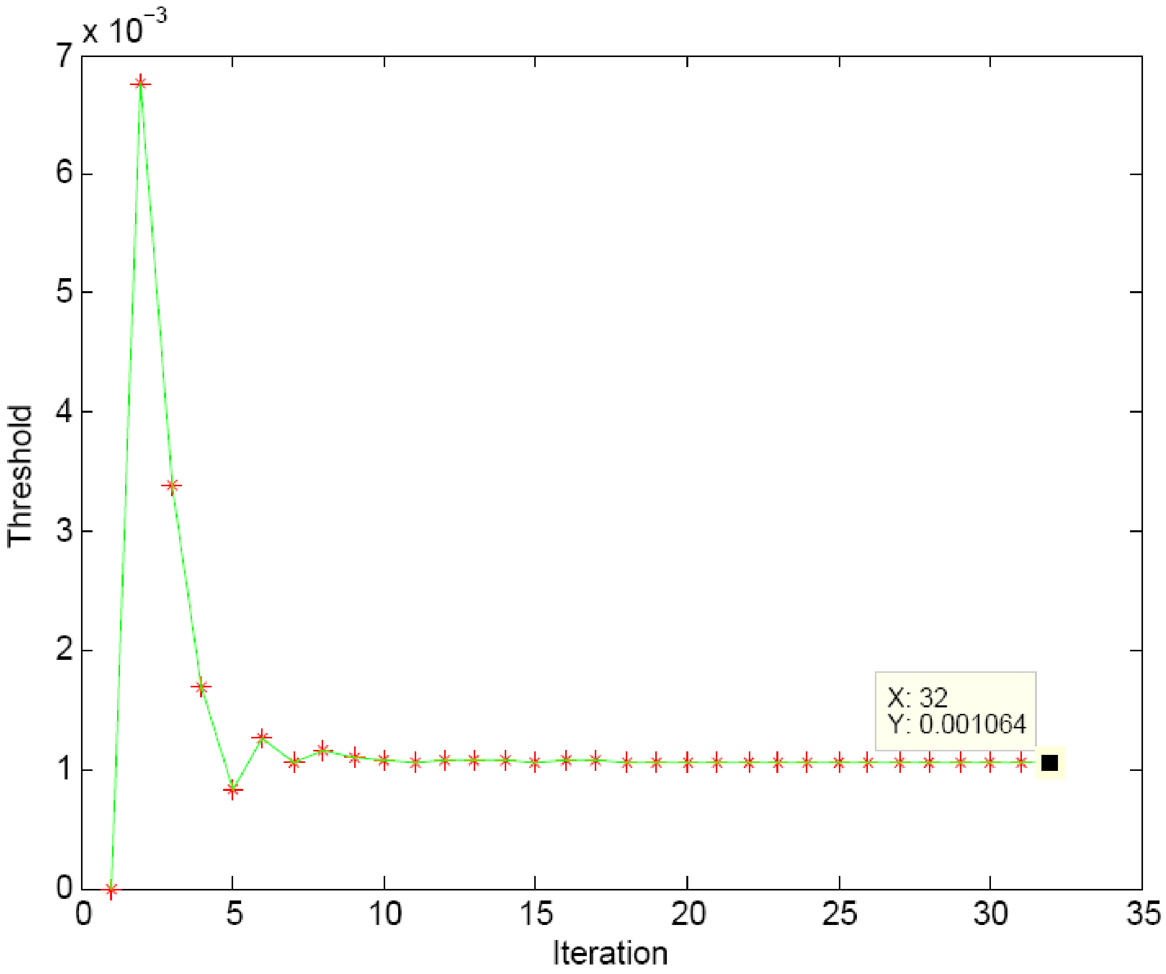

Figure 4.11: Threshold value at different iterations using bisection method

CHAPTER 5

This chapter presents simulation and experimental results that illustrate the effectiveness of the algorithm for fever subject's identification. Simulated thermal images were created to test the robustness of the procedure with respect to several critical scenarios, especially those involving the presence of different radiating sources other than face regions in the field of view of the camera. Offline implementation of the algorithm with thermal images acquired by an infrared camera is also shown.

5 Illustration of the algorithm using simulated images

5.1 Objects used in simulations

As a first step to simulate thermal images, different shapes characterizing typical face features and non-face features were obtained from online infrared image sources [30,44]. Infrared images are then converted into binary images with pixel values 1 (white) and 0 (black). A method to convert RGB images into binary images is described in section (4.1.1) of chapter (4). Some of the binary shapes used in the simulations are shown in Figure 5.1.

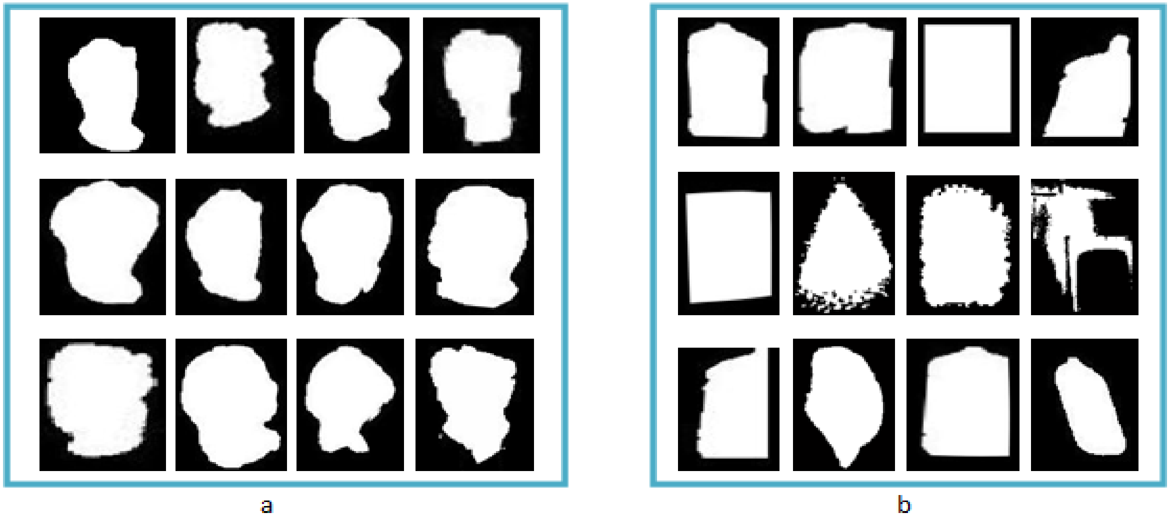

Figure 5.1: Binary images of (a) faces and (b) non faces.

5.1.1 Image Background

Both face and non face shapes as shown in Figure 5.1 are then used to obtain composite images with at least two face shapes and one heat source in a single image in order to simulate scenarios with multiple subjects. This is done by positioning the shapes obtained previously on a black background with dimension (350×450). A total of seventy images were built with face and non face shapes, and only some of them shown in Figure 5.2.

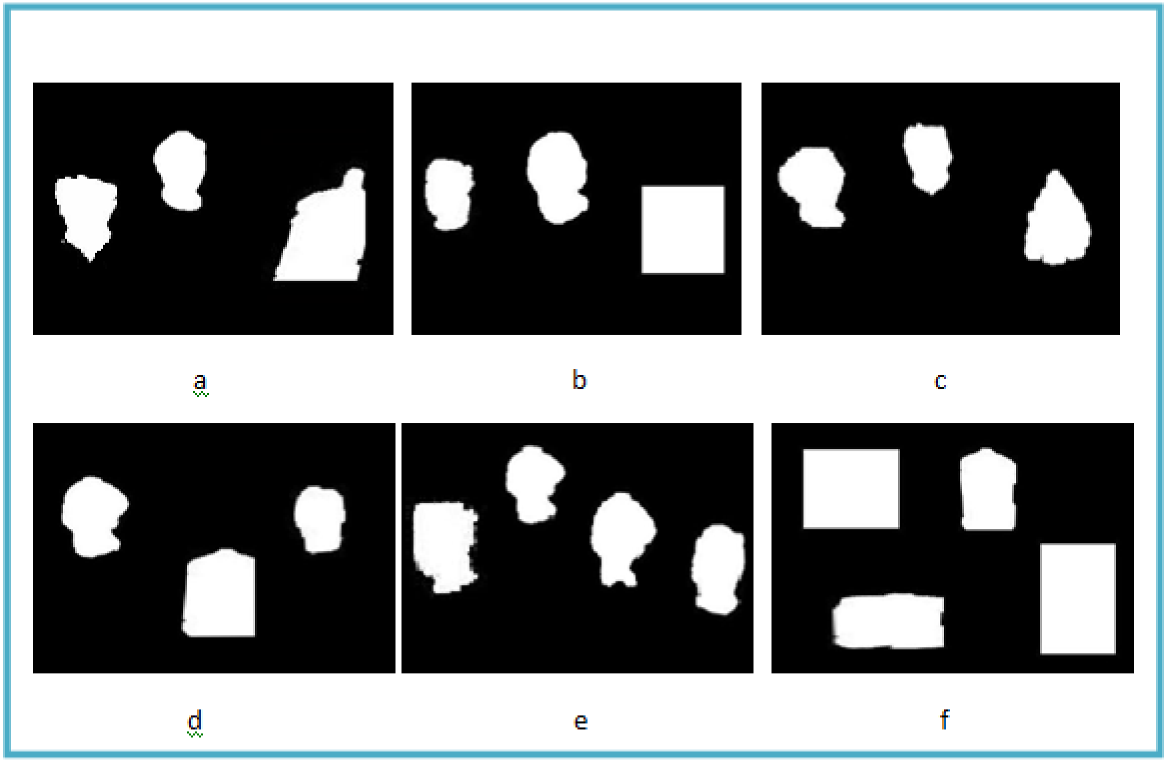

Figure 5.2: (a-f) Simulated binary images with face and non face shapes.

5.2 Implementation of the algorithm on simulated images

Different images built in the previous section are used to test the algorithm proposed in chapter 3. The process of implementation is shown in Figure 5.3.

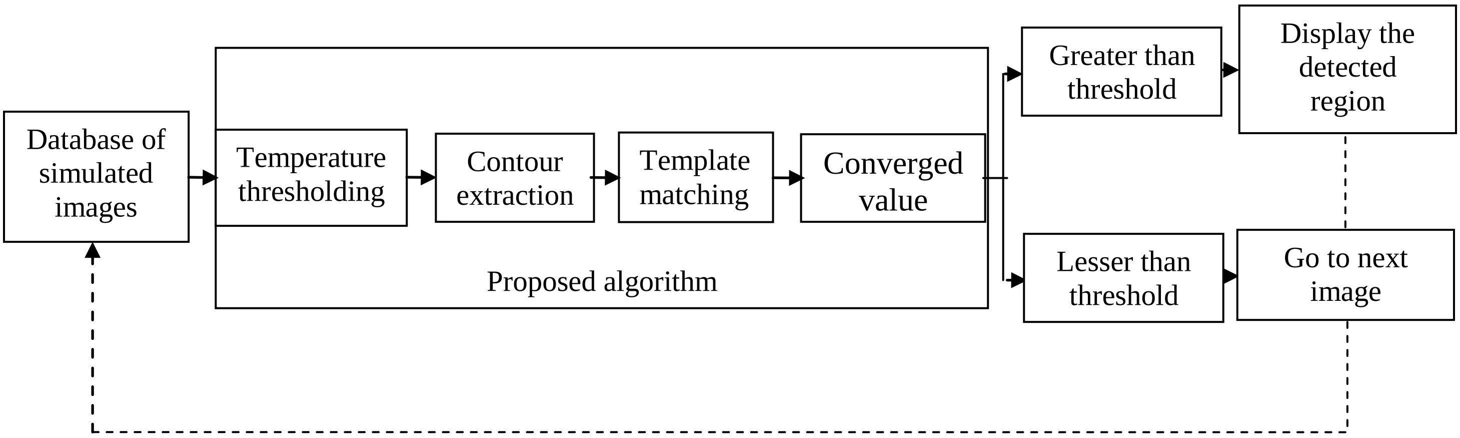

Figure 5.3: Process of testing proposed algorithm using simulated images.

As seen in Figure 5.3, the process involves different steps to establish the presence of possible face regions. Steps involved include temperature thresholding, contour extraction, template matching and Neyman-Pearson testing. The algorithm is processed on all the simulated images stored in a folder in an iterative manner. It stops and displays the detected regions (if any) and then goes back to the next image, until all the images are processed. Details of the implementation and actions of the algorithm in some representative images are shown in the next section.

5.2.1 Step by step application of the algorithm to a simulated image

Processing of the input image at different stages of the algorithm is presented in this section. One of the simulated images used as an input to the algorithm is shown in Figure 5.4. As we can observe in Figure 5.4, only face shapes were used and we did not consider any body region, this is because the human body region covered with the clothes radiate less than the face region and can be filtered out from the images through the first step temperature thresholding. This is shown in Figure 4.2, were it can be clearly seen that the body region (with less radiation) is filtered out from the image after temperature thresholding step.

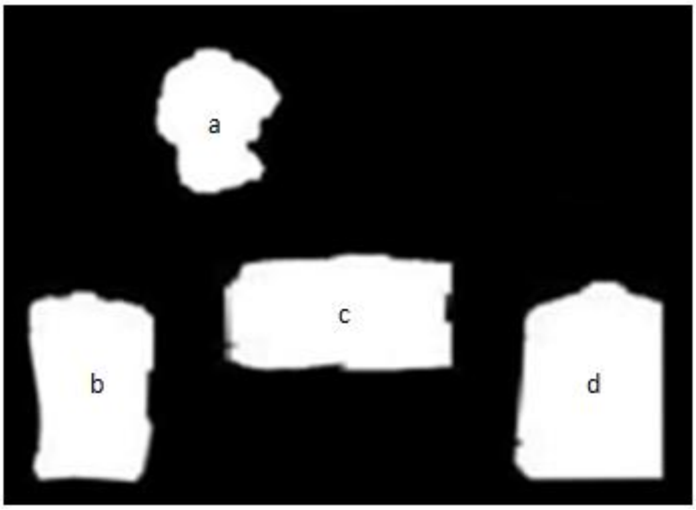

Figure 5.4: Binary image with four objects (a-d).

Contour extraction

Contours representing shapes of the objects (a-d) in Figure 5.4 are extracted in this step. The process of contour extraction is explained in detail in section (4.1.4). Contours obtained in this step are shown in Figure 5.5.

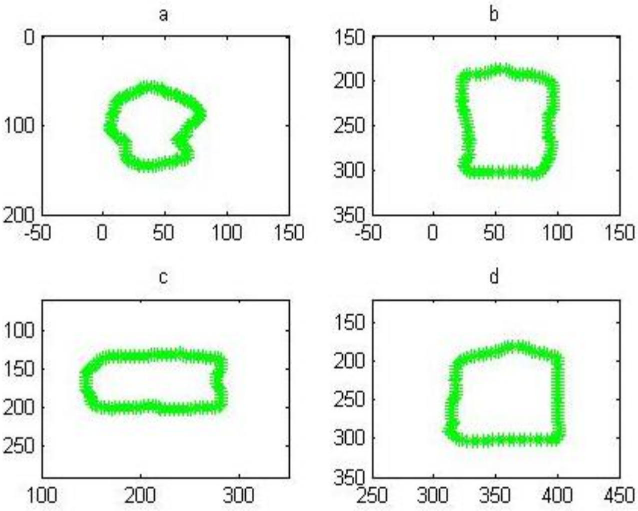

Figure 5.5: Contours of the objects (a-d) in Figure 5.4.

Template matching

In this step a template (circle) is deformed to match (in the sense of minimizing a suitable least square distance, see Chapter 4) the contours extracted in previous step. Template matching is explained in detail in section (4.2). Template converged to best fit contours (a-d) in Figure 5.5 and the converged values of the least square distances are shown in Table 5.1. Converged values obtained are then processed using the log likelihood ratio as in equation (4.6), which is designed to distinguish between face and non face shapes within the Neyman-Pearson decision making criterion. Recalling equation (4.6):

$$\Lambda(E) = -\left(\frac{E-\mu_1}{\sigma_1}\right)^2 + \left(\frac{E-\mu_0}{\sigma_0}\right)^2 \gtrless \gamma \tag{5.1}$$

where parameters μ_1, μ_0, σ_1 and σ_0 are given in Table 4.1 and the threshold value is $\gamma = 0.0011$, (see Figure 4.10). Values of the converged least square distances E corresponding to the contours in Figure 5.5 are given in Table 5.1

Converged template	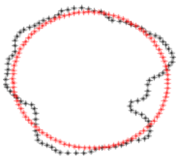	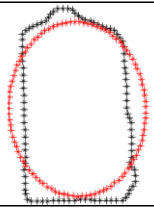	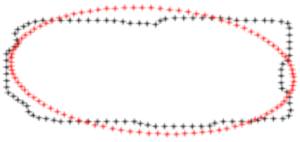	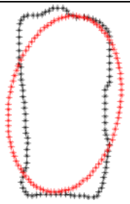
Converged value	3.10×10^{-4}	3.98×10^{-4}	4.02×10^{-4}	4.17×10^{-5}
$\Lambda(E)$	0.8551	-1.5957	-1.7282	-3.1166

Table 5.1: The template (red "*") converged with the contours of objects (a-d) (black "*"), and the corresponding converged and $\Lambda(E)$ values are also shown.

As shown in Table 5.1 the value of $\Lambda(E)$corresponding to the contour of the face is above the threshold value (0.0011) and values of the log-likelihood ratio $\Lambda(E)$ of the non face contours (b-d) are below the threshold. The face region with fever is correctly recognized from the input image and is displayed as the output using the algorithm as shown in Figure 5.6.

Figure 5.6: The detected face region.

It can be observed that the pixel values corresponding to the face regions with normal temperatures and the background are filtered in the first step, leaving face regions with fever and other non-face regions to the next step, which is dedicated to geometric recognition. In the following sections results of the template matching and testing steps corresponding to the different face shapes and non-face shapes extracted from simulated images are presented.

5.3 Template matching from several extracted contours

Converged deformed shapes resulting from template matching of all the face shapes with and non-face shapes extracted from the simulated images from Figure 5.2 are shown in Figure 5.7 and Figure 5.8, respectively. In the following figures, converged deformed templates are represented by red points and face and non-face contours extracted from images are represented by black points.

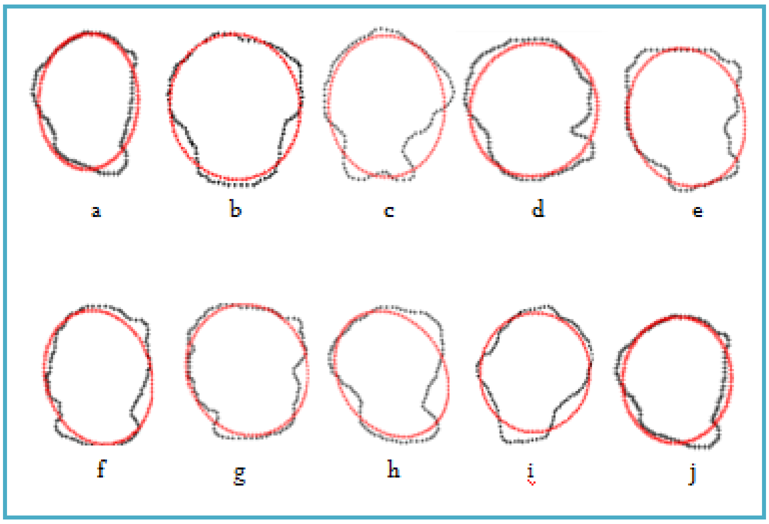

Figure 5.7: (a-j) Template (red) converged with the face shapes (black).

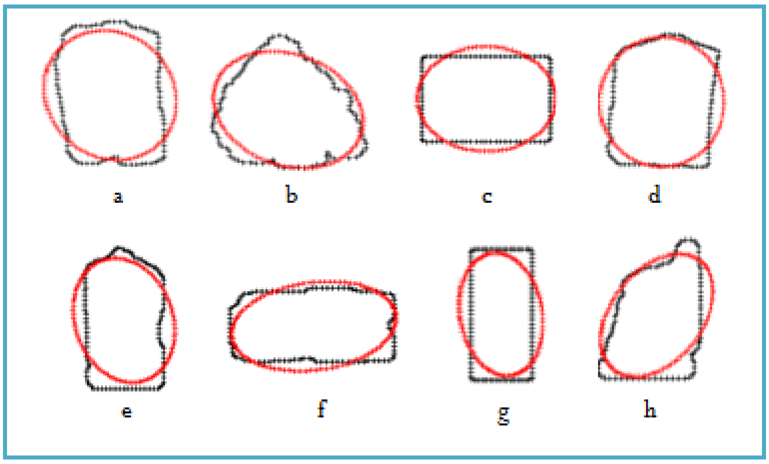

Figure 5.8: (a-i) Template (red) converged with the non-face shapes (black).

Converged minimum least square values and corresponding likelihood ratios corresponding to all the shapes in Figure 5.7 and Figure 5.8 are given in Table 5.2 and Table 5.3.

Face shapes	Converged value
a	2.16×10^{-4}
b	1.37×10^{-4}
c	3.89×10^{-4}
d	3.09×10^{-4}
e	2.66×10^{-4}
f	2.11×10^{-5}
g	1.62×10^{-4}
h	3.83×10^{-4}
i	2.95×10^{-4}
j	2.01×10^{-4}

(a)

Non face shapes	Converged value
a	4.12×10^{-4}
b	3.39×10^{-4}
c	3.63×10^{-4}
d	3.84×10^{-4}
e	3.93×10^{-4}
f	4.01×10^{-5}
g	4.23×10^{-4}
h	4.60×10^{-4}

(b)

Table 5.2: Converged values corresponding to the (a) face shapes and (b) non face shapes.

Face shapes	Likelihood ratios $\Lambda(E)$
a	2.4909
b	3.0810
c	-1.3042
d	0.8779
e	1.7471
f	2.5495
g	2.9718
h	-1.1307
i	1.1842
j	2.6581

(a)

Non face shapes	Likelihood ratios $\Lambda(E)$
a	-2.0676
b	0.1457
c	-1.5144
d	-1.1463
e	-1.4326
f	-1.6949
g	-2.4541
h	-3.8563

(b)

Table 5.3: Likelihood ratios corresponding to the (a) face shapes and (b) non-face shapes.

5.4 Statistical assessment using simulated images

In order to obtain some global indicator of the performance of the algorithm for face recognition we calculated the frequencies of occurrence of the following quantities on the population of seventy simulated images:

- False detection: The number of non-face shapes falsely detected as face shapes with fever temperatures.
- Detection: The number of face shapes with fever temperature correctly detected.
- Miss detection: The number of face shapes with fever not detected.
- Correct rejection: The number of non-face shapes correctly rejected.

The log-likelihood values for all the face and non-face shapes above threshold temperature extracted from 70 simulated images are plotted in Figure 5.9. The values corresponding to the face shapes are represented by red points while the values corresponding to non-face shapes are represented by green points. Blue line in the same figure represents the threshold value $\gamma = 0.0011$. The four parameters considered above correspond, respectively, to a green point above the threshold (False detection), a red point above the threshold (Detection), a red point below the threshold (Miss Detection), and a green point below the threshold (Correct rejection).

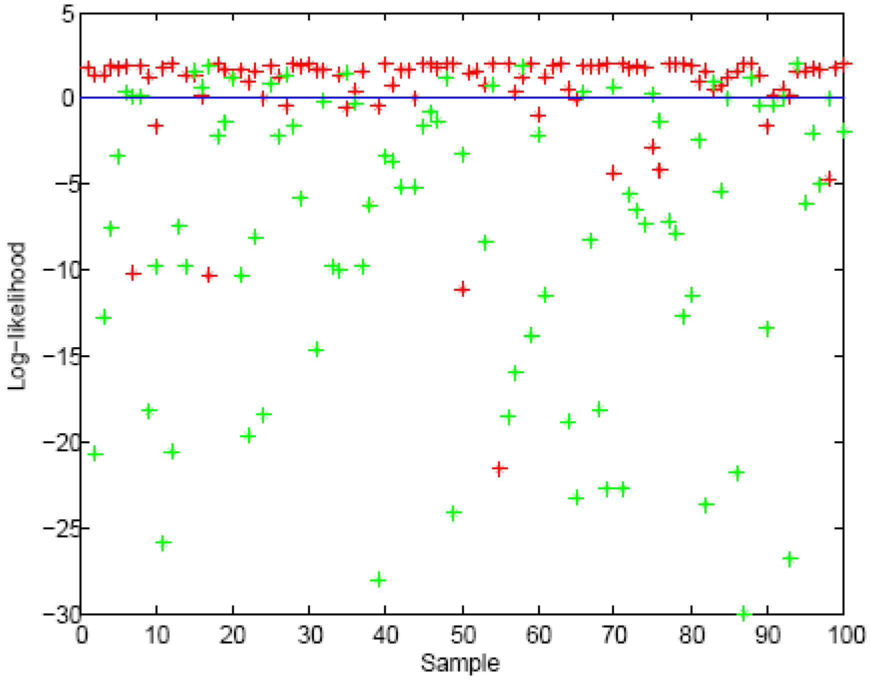

Figure 5.9: Log-likelihood values of face shapes (red dots) and non-face shapes (green dots). Blue line is the threshold value (0.0011).

Corresponding frequencies are listed in Table 5.4.

	False detection	Detection	Miss detection	Correct rejection
Frequency	0.20	0.82	0.18	0.80

Table 5.4: Frequencies of the four probabilistic indicators.

As expected, Detection and Miss detection are complementary with respect to 1, as it is the case for the pair False Detection and Correct rejection. The probability of False detection set to build the threshold is 0.05, corresponding to a probability of detection of 0.85. The discrepancy between frequency and probability is due to the fact that frequency values become good representation of probabilities when the size of the population is sufficiently large. Moreover, to compute the threshold the discrete distributions of converged minimum least square distances were replaced by Gaussian distributions with the same moments, which introduce an additional approximation.

5.5 Illustration of the algorithm on images acquired with an infrared camera

In this section we show results obtained on images acquired with an infrared camera. Experimental scenarios are designed based on few cases of simulated images. The following sections include experimental procedure, image capturing, processing and comparison of the results with the simulation results was discussed.

5.5.1 Objects used

Animated and not animated objects used in the experiments and the range of their respective temperatures are given in Table 5.5

Objects	Temperature
Normal person	33-36 ^{O}C
Emulation of fever	37-40 ^{O}C
Rectangular containers	37-42 ^{O}C
Square containers	37-42 ^{O}C
Reference temperature	36.5 ^{O}C

Table 5.5: Objects used in experiments and their temperatures.

Experiments were carried out in a closed room with ambient temperature of 26 ^{O}C. The scanner used was handheld thermal camera WAHL HSI3000 system, focal length from the subject to the scanner was 2-4 m. The detector used is an advanced high resolution(160×120) with 19,200 pixels and with a thermal sensitivity of 0.1℃ at 23℃. Spectral range of the scanner is between 8 to 14µm, with a measurement accuracy of ±2% real time reading. Thermal scanner and the objects used in the experiments are shown in Figure 5.10.

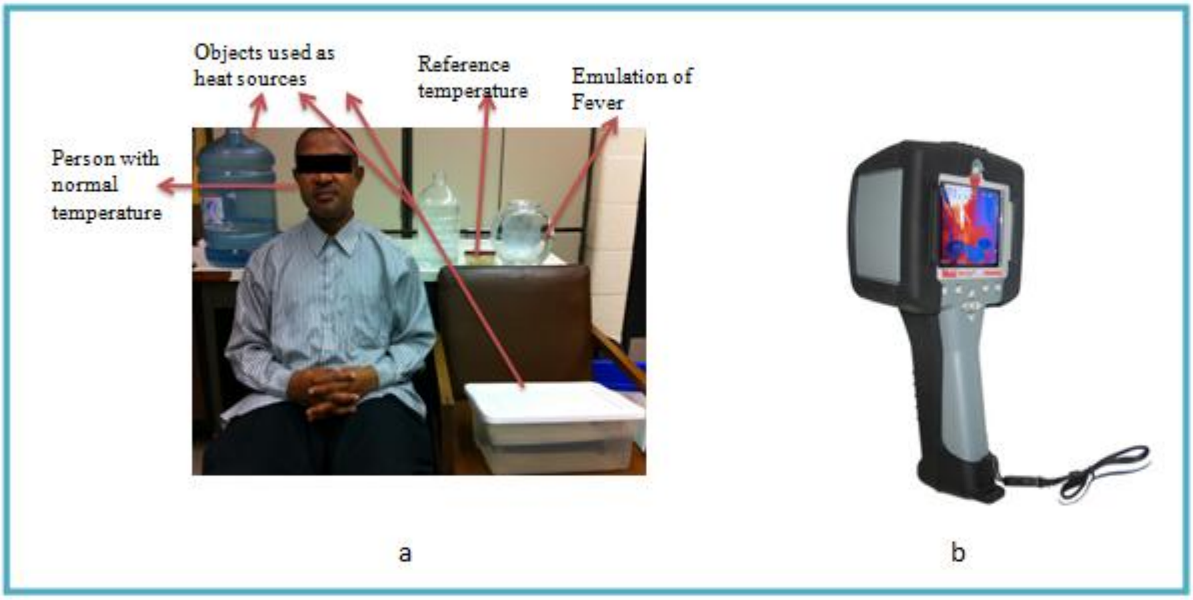

Figure 5.10: (a) Objects used in the experiments. (b) Infrared camera used in experiments.

An quasi-elliptical shaped container with water at different fever range temperatures as given in table is used to emulate a face with fever. Rectangular and square shaped containers are used as the radiating sources (reflecting the non-face shapes). Objects shown in Figure 5.10a are filled with water at desired temperatures (as shown in Table 5.5). Temperature of the water is constantly monitored using a thermometer to check if they vary from the desired temperatures. Figure 5.10b shows the hand held thermal camera used in the experiment.

5.5.2 Reference temperature

A small container as shown in Figure 5.10a maintained with water maintained at temperature 36.5 ^{O}C [11] is used as a reference temperature. The reference temperature is used as a discriminate between the normal and fever temperatures. This helps us further in temperature thresholding step (shown in section 4.1.1) to filter the objects in images which are less than the threshold temperature.

Different combinations of temperatures and heat sources are used in experiments to obtain images (similar to some simulated images in section 5.1). An outline of the set of combinations used for the experiments is shown in Table (5-6).

5.5.3 Experimental scenarios

Ten different combinations of objects are used in the experiments as outlined in Table 5.6. The experimental include few scenarios without any radiating heat sources, i.e. only human with normal temperature and emulated fever object. Other scenarios include more than one radiating heat sources with different temperatures as shown in Table 5.6 (#7, 8, 9, and 10).

Image #1			Image #7	
Normal individual	35 ^{O}C		Normal	35 ^{O}C
Image #2			Fever	38 ^{O}C
Fever	37 ^{O}C		Rectangular containers	37 & 42 ^{O}C
Image #3			Square container	35 ^{O}C
Normal	35 ^{O}C		Image #8	
Fever	38^{O}C		Normal	35 ^{O}C
Image #4			Fever	38 ^{O}C
Normal	35 ^{O}C		Rectangular containers	37, 39 & 42 ^{O}C
Fever	40 ^{O}C		Image #9	
Image #5			Normal	35 ^{O}C
Normal	35 ^{O}C		Fever	40^{O}C
Fever	37 ^{O}C		Rectangular containers	37, 38, 40, 42^{O}C
Rectangular	39 ^{O}C		Image #10	
Image #6			Normal	35 ^{O}C
Normal	35 ^{O}C		Fever	40 ^{O}C
Fever	38^{O}C		Rectangular containers	38, 40 & 42^{O}C
Rectangular container	42^{O}C		Square container	40 ^{O}C

Table 5.6: Outline of the experimental scenarios.

Experimental images obtained using infrared camera (Palmer Wahl) for the scenarios outlined in Table 5.6 are shown in the following section.

5.5.4 Experimental images acquired with the infrared camera

Images obtained for the combinations in Table 5.6 are as follows:

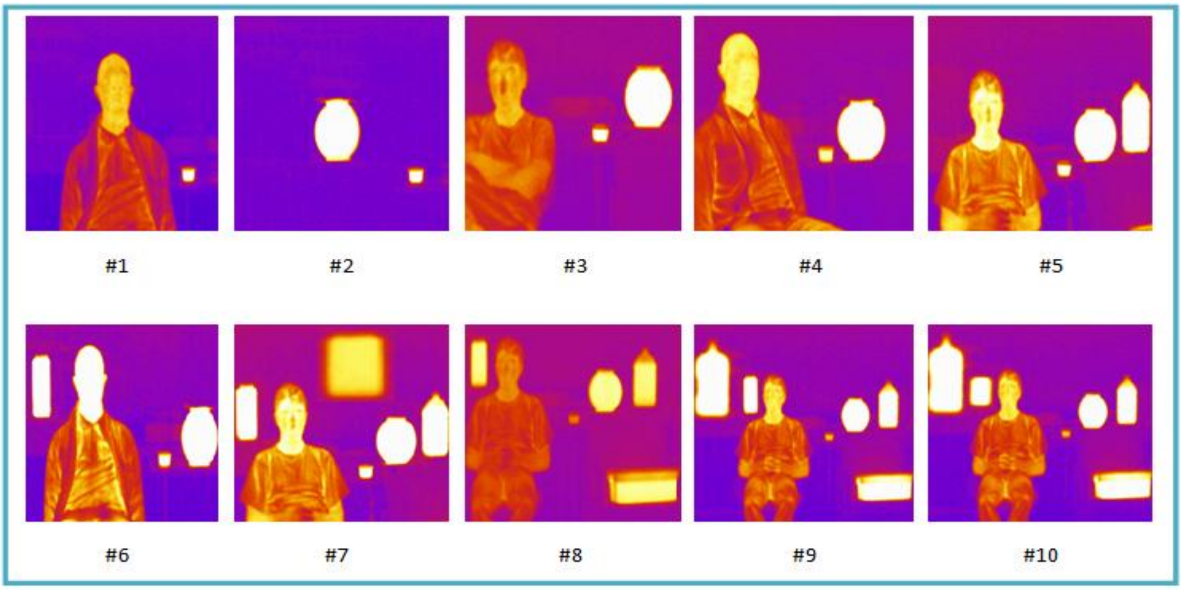

Figure 5.11: Thermal images obtained through experiments.

5.5.5 Experimental results and discussion

5.5.5.1 Testing the algorithm on image #8 in figure (5-11)

Processing one of the experimental image (#8) in Figure 5.11 (similar simulation image is shown in Figure 5.4) with detailed explanation of different stages of the algorithm is presented in this section with illustration purposes. The same procedure is applied to the other images and overall results are shown below.

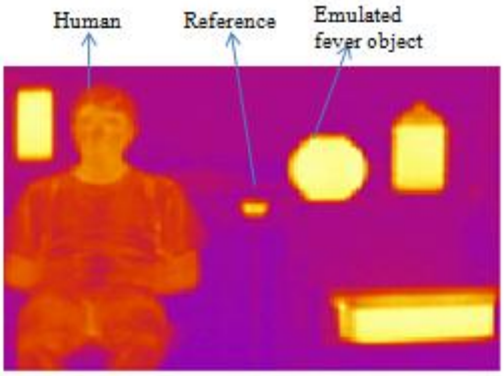

Figure 5.12: Thermal image showing normal person (without fever), oval region representing a face with fever, reference temperature and other radiating heat sources.

Temperature thresholding

Temperature thresholding is done by setting as threshold the average pixel intensity value corresponding to the temperature of the reference source, and by filtering the objects in the image with pixel intensity values less than the threshold. In this step the pixel values in the image less than the threshold are assigned 0(black) and values above are assigned 1(white). Image after temperature thresholding is shown in Figure 5.13.

Figure 5.13: Thermal image after temperature thresholding.

Contour extraction

Contours representing shapes of the objects in Figure 5.13 will be extracted. The process of contour extraction is explained in detail in section (4.1.4). Contours obtained in this step are shown in Figure 5.14.

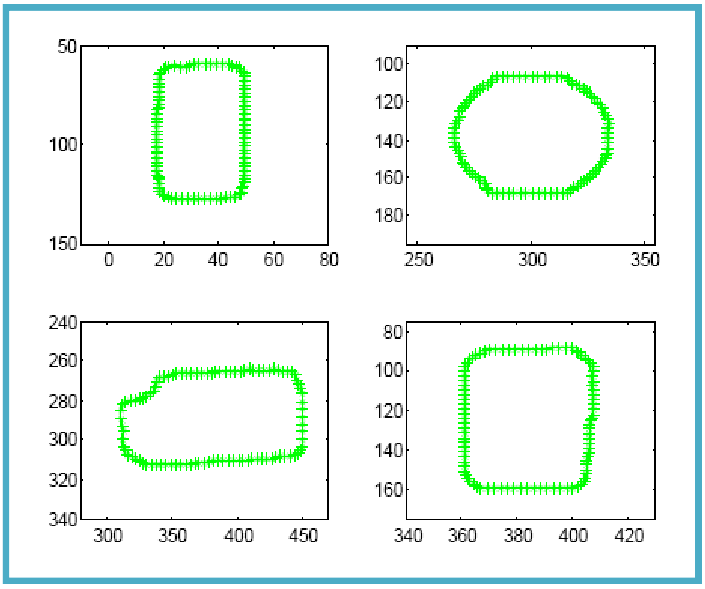

Figure 5.14: Contours of the objects in Figure 5-15.

Template matching

In this step a reference template (circle) is deformed to match (minimize the least square distance as explained in Chapter 4) the extracted contours. Template matching step is explained in detail in section (4.2). Converged deformed shapes in Figure 5.14 with the corresponding minimum least square distances and log-likelihood ratios reported in Table 5.7.

Converged template	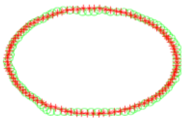	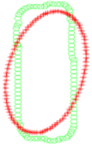	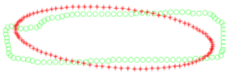	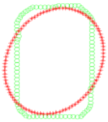
Converged value	3.9307×10^{-5}	5.3447×10^{-4}	5.8806×10^{-4}	4.7335×10^{-4}
Log-Likelihood ratio	2.8197	-6.9391	-9.4855	-4.2622

Table 5.7: Converged deformed template (red points) matching the contours of objects in Figure 5.14, and corresponding minimum least square distances and log-likelihood ratios.

As shown in Table 5.7 the log-likelihood ratio value corresponding to the contour of the face is above the threshold value (0.0011) and log-likelihood ratios of the non-face contours are below the threshold. The object representing a human face with fever is correctly recognized from the input image and is displayed as the output of the algorithm as shown in Figure 5.15.

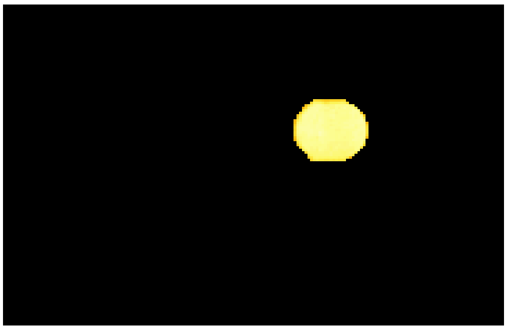

Figure 5.15: Showing the detected face region with fever.

5.5.5.2 Testing the algorithm on image #9 in figure (5-11)

We illustrate the algorithm by testing it on another image. The steps are the same as above.

Input image

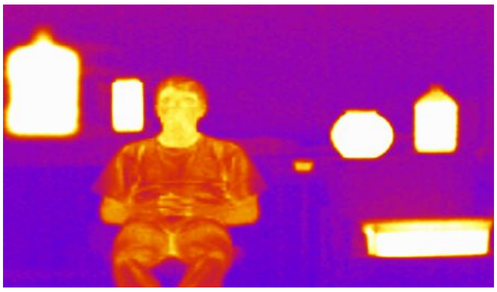

Figure 5.16: Input image #9

Template matching

Converged template	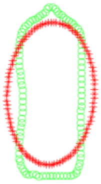	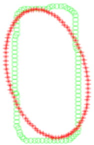	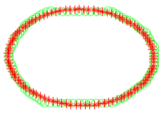	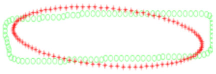	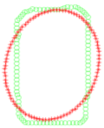
Converged value	6.2036×10^{-4}	4.8684×10^{-4}	4.0177×10^{-5}	4.9935×10^{-4}	4.6524×10^{-4}
Log-Likelihood ratio	-11.7294	-4.6797	2.8254	-5.1086	-3.8563

Table 5.8: Converged deformed template (red dots) matching the contours of objects in Figure 5.16, and the corresponding minimum least square distances and log-likelihood ratios.

Output

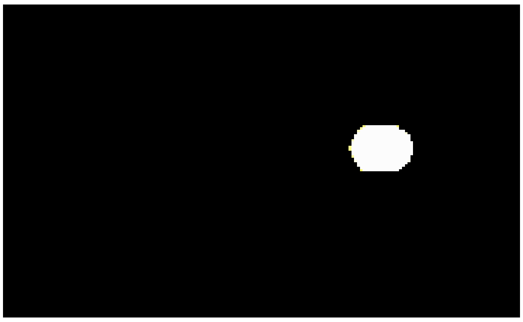

Figure 5.17: Output of the algorithm for the input image #9.

5.5.5.3 Testing the algorithm on image #10 in figure (5-11)

Input image

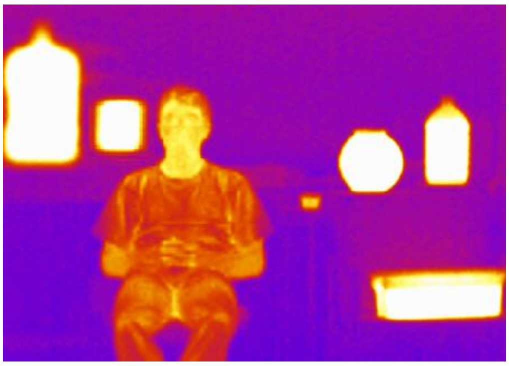

Figure 5.18: Input image #10

Template matching

Converged template	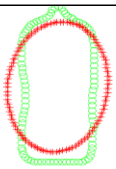	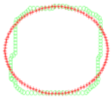	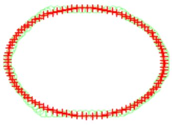	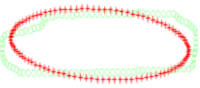	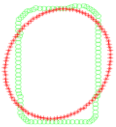
Converged value	6.5116×10^{-4}	2.5608×10^{-4}	4.1173×10^{-5}	4.2842×10^{-4}	4.8371×10^{-4}
Log-Likelihood ratio	-13.5328	2.0164	2.8336	-2.3474	-4.6797

Table 5.9: Converged deformed template (red dots) matching the contours of objects in Figure 5.18, and the corresponding minimum least square distances and log-likelihood ratios.

Output:

Figure 5.19: Output of the algorithm for the input image #9.

The output of image #10 in Figure 5.19 is the illustration of a case of false detection, in which a radiating non-face source was wrongly identified as a face region with fever. The heat source falsely detected is a square shaped object. It can be observed from the simulations that the converged values in the case of square shaped objects is often proximal to the threshold(table 6-4b (g)) and therefore changes in their shapes as for example curved corners can lead to converged least square distances that are wrongly associated with ovals by the algorithm.

Chapter 6

6 Conclusions and Future work

6.1 Overall Conclusions

The focus of this thesis was to develop an algorithm to automatically identify face regions with fever temperatures from infrared images. The developed algorithm was first tested on a training data constituted of 40 face and 40 non-face shapes to obtain probability distributions representing the two cases. The probability distributions are used to obtain the threshold from Neyman-Pearson based hypothesis testing. The threshold was determined for 5% false detection rate, corresponding to 85% probability of detection.

Using the obtained threshold value the algorithm was illustrated through testing with 70 simulated images and with 10 images acquired by an infrared camera. Simulated and experimental conditions reproduced several relevant scenarios characterizing crowded places. Frequencies of detection and false alarm rates were calculated by testing the algorithm on 70 simulated images, where we obtained a detection rate of 82% and false alarm rate of 20%.

6.2 Future work

One of the important step in the proposed algorithm is the decision making process, where we used 40 face and 40 non-face shapes to obtain a threshold value, to be used in the implementation of Neyman-Pearson based hypothesis testing. The threshold value obtained using the small number of database may not be reliable. Therefore increasing the number of face and non-face shapes in the training database is a key consideration for the future work.

The key motivation of this work is to achieve accurate detection of fever subjects during mass screening of moving people. As a first step towards the goal we illustrated the proposed algorithm using simulated and experimental images which reproduced several relevant scenarios of crowded places. The testing of the simulated and experimental images was carried out offline, and also the fever persons are not involved in our experiments (instead an emulation of fever person was used). Feature testing of the algorithm will involve the inclusion of more shapes in the training database to obtain the threshold value, and to test the algorithm with experiments involving more subjects (with fever, non-fever and external radiators).

6.2.1 Experimental considerations

A preliminary experiment setup was discussed in this thesis, however there are certain factors that can be considered to improve the proposed setup such as:

- Increasing the number of persons (with fever and normal temperatures),
- Increasing the number of heat sources.
- Using a temperature controlled reference plate (reference temperature).

6.2.1.1 Type of infrared camera

The type of camera used in this thesis is a handheld infrared camera. One of its main drawbacks is the unstable field of view, due to which the position of the reference plate within the images changes regularly. To address this issue, infrared camera mounted at a fixed position is recommended for future experiments.

REFERENCES

[1] Waldemar Minkina and Sebastian Dudzik., “Infrared thermography errors and uncertainities,” Wiley, ch.2, Nov 23, pp.15-20, 2009.

[2] Francis Ring, E. Ammer, Kurt, “Standard procedures for infrared imaging in medicine”, Medical Devices and Systems, pp.332-339, Apr. 2006.

[3] Lung-Sang Chan, Giselle T. Y. Cheung, Ian J. Lauder, and Cyrus R. Kumana, “ Screening of fever by remote sensing infrared thermographic camera,” J Travel Med, vol. 11, pp. 273-279, 2004.

[4] Ng. E. Acharya, "Remote-sensing infrared thermography," Engineering in Medicine and biology magazine, IEEE, vol. 28, pp. 76-83, Jan-Feb, 2009.

[5] X. Maldague, “Theory and Practice of IR Technology for Non destructive Testing,” Wiley, ch.2, pp.20-25, 2001.

[6] G. Gaussorgues, “Infrared thermography,” Springer, Technology and engineering, ch.1, pp.5-15, 1994.

[7] Acetta J.S. and D. L. Shumaker, “The Infrared and Electro-Optical Systems Handbook,” Vol. 4, SPIE Optical Engineering Press, Bellingham, Washington, pp.254-260, 1996.

[8] M. Vollmer, M. Klaus-Peter, “Infrared thermal imaging: Fundamentals, Research and applications,” John Wiley & Sons, Medical, Ch.1, pp.4-10, 2011.

[9] E. Y. K. Ng, ‘‘Is thermal scanner losing its bite in mass screening of fever due to SARS?,’’ Med. Phys, vol. 32, no. 1, pp. 93–97, 2005.

[10] Lung-Sang Chan, Giselle T. Y. Cheung, Ian J. Lauder, and Cyrus R. Kumana, “ Screening of fever by remote sensing infrared thermographic camera,” J Travel Med, vol. 11, pp. 273-279, 2004.

[11] Eddie Y. K. Ng, G. J. L. Kawb, W. M. Chang, “Analysis of IR thermal imager for mass blind fever screening”, Microvascular Research, Volume 68, Issue 2, pp. 104-109, September 2004.

[12] Y. H. Tan, C. W. Teo, E. Ong, L. B. Tan, and M. J. Soo, ‘‘Development anddeployment of infrared fever screening systems,’’ in Thermosense XXVI, Proc.SPIE, Orlando, USA, vol. 5405, pp. 68–78, 2004.

[13] L. Wang, S. Z. Chua, and V. Tan, ‘‘Types of thermal imaging systems for mass fever screening and their evaluations,’’ Thermosense XXVI, Proc. SPIE, Orlando, FL, vol. 5405, pp. 79–87, 2004.

[14] Ming-Fu Chiang, Po-Wei Lin, Li-Fong Lin, Hung-Yi Chiou, Ching-Wen Chien, Shu-FenChu, Wen-Ta Chiu6, “Mass screening of suspected febrile patients with remote-sensing infraredthermography: alarm temperature and optimal distance,” J Formos Med Assoc, vol. 107, no. 12, pp. 937-944, 2008.

[15] W. T. Chiu, P. W. Lin, H. Y. Chiou, W. S. Lee, C. N. Lee, Y. Y. Yang, H.M. Lee, M. S. Hsieh, C. J. Hu, Y. S. Ho, W. P. Deng, and C. Y. Hsu, ‘‘Infraredthermography to mass-screen suspected SARS patients with fever,’’ Asia Pac. J.Public Health, vol. 17, no. 1, pp. 26–28, 2005.

[16] L. J. Jiang, E. Y. K. Ng, A. C. B. Yeo, S. Wu, F. Pan, W. Y. Yau, J. H. Chen and Y. Yang, “A prespective on medical infrared imaging”, Journal of Medical Engineering & Technology, pp. 257-267, 2005.

[17] http://www.optotherm.com/ts-infrared-fever-screen-brochure.pdf.

[18]http://www.flir.com/uploadedFiles/Thermography_APAC/Products/Product_Literture/Swine%20-%20A320.pdf%20[11%20May].pdf.

[19] S. Sumriddetchkajorn and K. Chaitavon, “A non-invasive human temperature screening system with multiple detection points”, Proc. SPIE, 7003, 2008.

[20] Wang Xiaoyu, Chen Jihong, Wang Pingjiang, Huang Zhihong , "Infrared Human Face Auto Locating Based on SVM and A Smart Thermal Biometrics System," Intelligent Systems Design and Applications, Sixth International Conference , vol.2, pp.1066-1072, 16-18 Oct. 2006.

[21] Sumriddetchkajorn. S and Chaitavon. K. ,“Field test studies of our infrared-based human temperature screening systemembedded with a parallel measurement approach,” Infrared Physics and Technology, vol.52 (4), pp. 119-123, 2009.

[22] Pavlidis, I and Symosek, P, "The imaging issue in an automatic face/disguise detection ystem ," Computer Vision Beyond the Visible Spectrum: Methods and Applications, IEEE workshop, vol.2, pp.15-24, 2000.

[23] Chai Quek, W. Irawan, E. Y. K. Ng, “A novel brain-inspired neural cognitive approach to SARS thermal image analysis,” Expert Syst. Appl., vol.37(4), pp. 3040-3054, 2010.

[24] Yoshitomi. Y, Miyaura. T, Tomita. S, Kimura. S, "Face identification using thermal image processing," Robot and Human Communication, 1997. RO-MAN '97 Proceedings, 6th IEEE International Workshop on , vol. 2, pp.374-379, 29 Sep-1 Oct 1997.

[25] A. Srivastava and X. Liu, “Statistical hypothesis pruning for identifyingfaces from infrared images,” J. Image Vision Comput., vol. 21, no. 7, pp.651–660, 2003.

[26] R.Brunelli, “Template matching techniques in computer vision”, Wiley, ch-3, 2008.

[27] C. Yao, J.A. Kovacs, and W. Wriggers, “2D fast rotational matching forimage processing of biophysical data”, J StructBiol, vol.144, pp.51–60, 2004.

[28] H. Keipke, “Overview of image matching techniques, research report of lehrstuhlfur photogrammetrie und fernerkunduny,” Technische University Munchen,April 29, 1996.

[29] S. Theodoridis and K. Koutroumbas, “Pattern recognition,” 2nd edition, AcademicPress, pp.481–512, 2003.

[30] http://www.terravic.com/research/facial.htm.

[31] Yuille. A.L, Cohen. D.S, Hallinan. P.W, "Feature extraction from faces using deformable templates," Computer Vision and Pattern Recognition, 1989. Proceedings CVPR ‘89., IEEE Computer Society Conference, vol.2, pp.104-109, 4-8 Jun 1989.

[32] P. Muse, F. Sur, F. Cao, Y. Gousseau, and J.M. Morel, “Accurateestimates of false alarm number in shape recognition,” TechnicalReport 5086, INRIA, 2004. Submitted.

[33] Zhong Xue, Dinggang Shen, Eam KhwangTeoh , "A deformable template model based on fuzzy alignment algorithm," Image Processing, Proceedings., International conference, vol.1, pp.296-299, 2008.

[34] Fernando Jorge, SoaresCarvalho, and João Manuel, “Eye detection using a deformable template in static images”, VIPimage - I ECCOMAS Thematic Conference on Computational Vision and Medical Image Processing, pp. 209-215, 2007.

[35] Burr, D.J., “Elastic matching of line drawings,” *IEEE Trans.*Patt. Anal.Mach. lntell.3(6), pp.708-713, 1998.

[36] James M.Palmer, Barbara G. Grant, “The art of radiometry,” SPIE, December 16, 2009.

[37] Ernest O. Doebelin “Measurement systems application and design,” fourth edition, McGraw-Hill, Inc, 1990.

[38] NiranjanKrishnamurthi, Shanchieh Jay Yang, “Feasibility and Performance Analysis of Sensor Modeling in OPNET,” Rochester Institute of Technology, 2007.

[39]Karl Erik Lonngren, Sava VasilevSavov, Randy J. Jost, “Fundamentals of electromagnetic with matlab,” Scitech, January 11, 2010.

[40] http://www.mathworks.com/help/toolbox/images/f18-12508.html.

[41] Edwin K.P and Stanislaw H.Z, “An introduction to optimization,” Wiley, ch-7, pp.312-330, 2008.

[42] Bertsekas, D. P., and Tsitsiklis, J. N, “Parallel and distributed computation: numerical methods,”. Prentice Hall, Englewood Cliffs, New Jersey, pp.124-129, 1989.

[43] P. Mus´e, F. Sur, F. Cao, Y. Gousseau, and J.M. Morel, “Accurateestimates of false alarm number in shape recognition,” TechnicalReport 5086, INRIA, 2004. Submitted.

[44] http://medicalir.com/component/joomgallery/?func=detail&id=300.

[45] Jain. A.K, Yu Zhong, Lakshmanan.S, "Object matching using deformable templates," Pattern Analysis and Machine Intelligence, IEEE Transactions on , vol.18, no.3, pp.267-278, Mar 1996.

[46] Eugene Hecht, “Optics fourth edition,” Addison Wesley, pp.192-200, August 12, 2001.

[47] Lipson, P, Yuille, A. L, O’Keefe, D, Cavanaugh, J, Taaffe, J. and Rosenthal, D. “Deformable templates for feature extraction from medical images”, In Faugeras, O. (ed.), Computer Vision – Proc. First European Conf. on Computer Vision (ECCV’90), Antibes, France, pp. 477–484, April. 1990.

[48] Susanna. R.D, Gillian. A.L, Jean. V.C, Rosalind. L.S, Paula. R.W, “In a systematic review, infrared ear thermometry for fever diagnosis in children finds poor sensitivity,” Journal of clinical epidemiology, Vol.59, pp.354-357, April 2006.

[49] http://www.nationalinfrared.com/image_browser.php.

[50] http://www.mathworks.com/help/toolbox/images/ref/imopen.html.